The influence of resolved convective motions on scalar dispersion in hectometric scale numerical weather prediction models

Received: 9 May 2023 | Revised: 3 October 2023 | Accepted: 22 November 2023

DOI: 10.1002/qj.4632

Quarterly Journal of the Royal Meteorological Society RMetS

RESEARCH ARTICLE

The influence of resolved convective motions on scalar dispersion in hectometric-scale numerical weather prediction models

Lewis P. Blunn[1,2,3] | **Robert S. Plant**[2] | **Omduth Coceal**[2,3] | **Sylvia I. Bohnenstengel**[1] | **Humphrey W. Lean**[1] | **Janet F. Barlow**[2]

[1]MetOffice@Reading, University of Reading, Reading, UK

[2]Department of Meteorology, University of Reading, Reading, UK

[3]National Centre for Atmospheric Science (NCAS), University of Reading, Reading, UK

Correspondence
Robert S. Plant, Department of Meteorology, University of Reading, Reading, RG6 6ET, UK.
Email: r.s.plant@reading.ac.uk

Abstract

The UK Met Office has a 300-m grid length numerical weather prediction (NWP) model running routinely over London and, in research mode, city-scale hectometric grid length NWP has become commonplace. It is important to understand how moving from kilometre- to hectometre-scale grid length NWP influences boundary-layer vertical mixing. For a clear-sky convective boundary layer (CBL) case study, using 55- and 100-m grid length NWP, we demonstrate that CBL vertical mixing of passive scalar is almost fully resolved. Passive scalar converges near the surface after emission from an idealised pollution ground source representing city-scale emissions, and is transported in updrafts preferentially into the upper boundary layer. Approximately 8 km downstream of the source edge, this causes 34% lower near-surface concentrations compared with 1.5-km grid length NWP, where vertical mixing is fully parameterised. This demonstrates that resolving ballistic-type dispersion, which is not typically represented in NWP vertical mixing parameterisations, can have a leading-order influence on city-scale near-surface pollution concentration. We present a simple analytical model that is able to capture diffusive and ballistic dispersion behaviour in terms of effective timescales. The timescale controlling how long it takes passive scalar to become well mixed in the CBL is ≈ 3 times longer for 1.5-km compared with 100- and 55-m grid length NWP.

KEYWORDS

air quality, city-scale, dispersion, hectometric, Lagrangian stochastic model

1 | INTRODUCTION

Over the past decade, several studies have evaluated kilometre- versus subkilometre-scale numerical weather prediction (NWP) for different meteorological applications (Belair et al., 2018; Boutle et al., 2016; Hagelin et al., 2014; Hanley et al., 2015; Hanley et al., 2016; Leroyer et al., 2014; Leroyer et al., 2022; Ronda et al., 2017). At subkilometre horizontal grid lengths (Δ) urban areas are better represented in NWP, and therefore these models are often referred to as "urban-scale". For $\Delta = \mathcal{O}(100\ \text{m})$, unlike $\Delta = \mathcal{O}(1\ \text{km})$, the majority of convective boundary layer (CBL) turbulence is resolved explicitly (Boutle et al., 2014; Honnert et al., 2020), and turbulent structures such as horizontal convective rolls (HCRs) are simulated (Lean et al., 2019). Until now, the influence of parameterising ($\Delta \geq \mathcal{O}(1\ \text{km})$) versus explicitly resolving CBL vertical mixing of passive scalars in NWP has not been investigated. This study assesses the potential improvements and changes in vertical mixing behaviour when moving from $\Delta = \mathcal{O}(1\ \text{km})$ to $\Delta = \mathcal{O}(100\ \text{m})$ NWP.

Turbulent dispersion of particles has two different behaviours at long and short times after release. In the long-time "diffusive" limit, defined as times greater than the order of a decorrelation timescale τ, dispersion is less efficient, since particles have lost memory of the initial eddy into which they were released. The particles undergo random motion, with the mean square displacement of particles increasing proportional to time (Taylor, 1922). In the short-time "ballistic" limit, particles travel at the velocity within the eddy they were released into, and the mean square displacement of particles increases proportional to the time squared (Taylor, 1922). First using large-eddy simulations (LES, Deardorff, 1972b), then using a water convection chamber experimentally (Willis & Deardorff, 1976), it was found that ballistic-type dispersion results in passive scalar having a "lift-off" behaviour when released near the surface. At times of the order of a convective eddy turnover time (t_*) (Deardorff, 1970; Lilly, 1968), particles have a larger likelihood of being in the upper than the lower half of the CBL, and there is a decrease in near-surface concentration.

Passive scalar dispersion in NWP can be used to understand aspects of pollution dispersion in air-quality models (AQMs), since chemical species in AQMs are treated as passive scalars when transported (Baklanov et al., 2014; Kukkonen et al., 2012; Warhaft, 2000). Also, like NWP, regional to global-scale AQMs generally use K theory (sometimes with an additional countergradient term) to parameterise turbulent mixing (Baklanov et al., 2014; Kukkonen et al., 2012), so results from NWP are applicable to AQMs. City-scale AQMs that resolve urban topography typically use advanced Gaussian plume-dispersion models (Cimorelli et al., 2005; McHugh et al., 1997; Stockie, 2011), which, like K-theory-based dispersion models, only represent diffusive-type dispersion. Exceptions to the rule are Lagrangian stochastic models (LSMs: Thomson & Wilson, 2012; Wilson & Sawford, 1996), such as the UK Met Office's Numerical Atmospheric-dispersion Modelling Environment (NAME) model (Webster & Thomson, 2018), which can incorporate ballistic-type dispersion.

Here, for the first time it is possible to evaluate city-scale CBL vertical mixing of passive scalar at $\Delta = \mathcal{O}(1\ \text{km})$ and $\Delta = \mathcal{O}(100\ \text{m})$ within one NWP framework (the UK Met Office Unified Model (MetUM)), enabling investigation of the implications for AQMs when ballistic-type dispersion is represented. Previous studies employing methods capable of representing both diffusive and ballistic dispersion have been for point sources or distributed sources, with study regions of limited streamwise extent. The size restriction is caused by computational cost (LES) or limited chamber size (experiments) (Deardorff, 1972b; Dosio et al., 2003, 2005; Gopalakrishnan & Avissar, 2000; Willis & Deardorff, 1976, 1981). Previous literature has therefore not explored the full city-scale downstream evolution of passive scalar from a city-scale ground source.

We study vertical mixing of continuous and puff-released passive scalar from a homogeneous ground-area source for a clear-sky CBL case study (May 4, 2016) at $\Delta = 55\ \text{m}$, 100 m, and 1.5 km. The idealised pollution emissions (i.e., passive scalar) are transported by NWP simulations that have fully realistic meteorology. Our research questions are the following.

- Is the three-dimensional spatial structure and evolution of the passive scalar field realistic in $\Delta = \mathcal{O}(100\ \text{m})$ NWP?
- Can a reduced analytical model capture timescales that characterise the different vertical mixing regimes in $\Delta = \mathcal{O}(1\ \text{km})$ and $\Delta = \mathcal{O}(100\ \text{m})$ NWP?
- Does resolving ballistic-type dispersion affect city-scale evolution of near-surface pollution concentration?

The article is structured as follows: Section 2 describes the case study, MetUM configurations, and passive scalar sources, Sections 3.1.1 and 3.1.2 analyse the CBL and passive scalar field structure in the vertical and horizontal, respectively, Section 3.2 interprets the vertical mixing dynamics qualitatively, Section 3.3 quantifies the vertical mixing behaviour with timescales from a reduced analytical model, Section 3.4 investigates the importance of ballistic-type dispersion on city-scale near-surface concentrations, Section 4 summarises and discusses the article's findings, and the Appendix A outlines the reduced analytical model.

2 | METHODS

2.1 | Case study

The chosen case study date is May 4, 2016. Southeast England was under a high-pressure system centred on continental Europe (Blunn, 2021). According to the London Urban Meteorological Observatory (LUMO: Kotthaus & Grimmond, 2014) it was a clear-sky day. This is based on the definition that at least three of the four ceilometers had no overhead cloud at any height more than 99% of the time. A clear-sky day was chosen since clear-sky conditions are conducive to strong CBL mixing. Also, they are the most simple conditions in which to study CBL mixing, since there is no influence from cloud-generated latent heating or turbulence.

At the University of Reading Atmospheric Observatory (URAO: ≈ 60 km west of Central London, 51.44°N, 0.94°W, blue cross in Figure 1a), the hourly-average 10-m wind direction was predominantly from the south between 0800 and 2200 UTC, varying between 165° and 203°, with a mean of 186°. Sensible heat flux (Q_H) observations were available from a network of three scintillometers separated by 1–3 km in Central London (Crawford et al., 2017). Between 1100 and 1500 UTC, hourly averaged Q_H was 300–400 W m^{-2} for the different scintillometer paths. At URAO the average 10-m wind speed was 2.8 m s^{-1} during the same period. Given the moderate wind speeds and large Q_H, the case date is suitable for the study of an archetypal CBL. The aim of this study is not an evaluation of the modelled convection, as Doppler lidar observations are not available, unlike in Lean et al. (2019).

2.2 | Model configuration

The MetUM (version 10.5) simulations are performed using a one-way nested research suite centred on London. See Table 1 and Figure 1a for the model configurations and domains, respectively. The simulations contain

TABLE 1 Model configurations.

Model	Horizontal grid length	Domain size (grid points)	Time step	Vertical levels
UKV	1.5 km	744 × 928	60 s	70
UM500	500 m	600 × 600	10 s	140
UM300	300 m	430 × 430	10 s	140
UM100	100 m	800 × 800	3 s	140
UM55	55 m	1440 × 1440	2 s	140

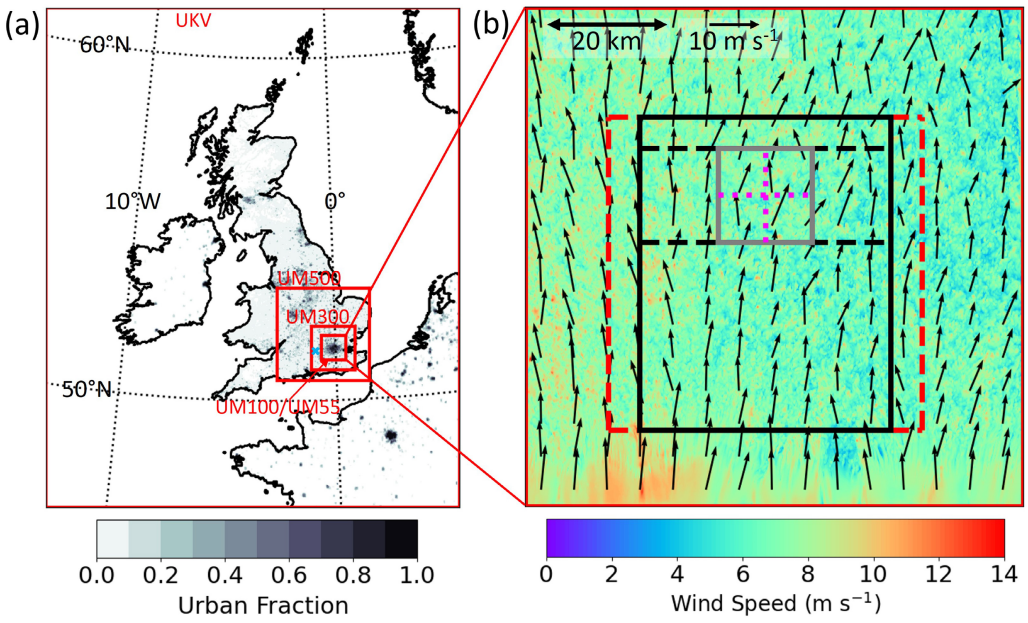

FIGURE 1 (a) Nesting suite schematic with urban fraction plotted. Each nest is highlighted in red. The outermost nest is UKV, and in decreasing domain size order the other nests are UM500, UM300, UM100, and UM55. UM100 and UM55 have the same domain size. URAO is highlighted with a blue cross and is just to the west of the UM100/UM55 domain. (b) UM55 wind-speed map at 1300 UTC at height 300 m. The arrows are wind vectors. Highlighted are the puff-release ground-source area (red solid line, around the full region displayed in (b)), continuous-release ground-source area (red dashed line), analysis region 1 (black dashed line), analysis region 2 (black solid line), horizontal cross-section location (grey solid line; Figure 4), west–east vertical cross-section location (horizontal magenta dotted line; Figure 3), and south–north vertical cross-section location (vertical magenta dotted line; Figure 6). [Colour figure can be viewed at wileyonlinelibrary.com]

idealised passive scalar emissions (see Section 2.3), but fully realistic meteorology (e.g., microphysics, orography, and land–atmosphere exchanges). The outermost nest is the variable-resolution UKV model (Tang et al., 2013) which has $\Delta = 1.5$ km over southeast England. Archived operational UKV model outputs are used to provide initialisation and hourly lateral boundary conditions (LBCs). The UKV nest provides LBCs to the $\Delta = 500$ m model (UM500), which passes LBCs to the $\Delta = 300$ m model (UM300), which finally passes LBCs to drive both the $\Delta = 100$ m (UM100) and $\Delta = 55$ m (UM55) models. LBCs for the 500–55 m models have a frequency of 15 min. The simulation start times are 0000 UTC for UKV and UM500, 0300 UTC for UM300, and 0600 UTC for UM100 and UM55, so that the time period common to all models is 0600–2200 UTC, allowing at least 5 hr for the turbulence to spin up in all of the models before the first model output analysis (1100 UTC).

Lean et al. (2019) used an almost identical UM nesting suite and tested a $\Delta = 100$ m model domain with $(30 \times 30\ \text{km})^2$ horizontal extent. Turbulence did not "spin up" until 10–15 km downstream of the inflow boundary. By extending the horizontal extent of the domain to $(80 \times 80\ \text{km})^2$, the turbulence had developed fully before it reached the London area (approximately $(50 \times 50\ \text{km})^2$). The case study was a clear-sky CBL like the one presented here, so the same $(80 \times 80\ \text{km})^2$ domain has been used for the 100- and 55-m models. The domain top in all models is at 40 km. A Charney–Phillips vertical grid is used where there are half levels (containing, e.g., horizontal velocities and pressure) that are staggered with full levels (containing, e.g., potential temperature, passive scalar, and vertical velocity). Spacing is quadratic so that there is higher vertical resolution within the boundary layer (BL) than above. UKV uses a 70 vertical level set, which has 23 full levels within the lowest 2 km at heights 5.0, 21.7, 45.0, and 75.0 m within the lowest 100 m, and the other models use a 140 vertical level set, which has 52 full levels within the lowest 2 km at heights 2.0, 5.3, 10.0, 16.0, 23.3, 32.0, 42.0, 53.3, 66.0, 80.0, and 95.3 m within the lowest 100 m.

The MetUM version 10.5 dynamical core ("ENDGame") solves fully compressible, nonhydrostatic, deep-atmosphere dynamics using a semi-implicit semi-Lagrangian (SISL) numerical scheme (Davies et al., 2005; Wood et al., 2014). The scale-aware blended boundary-layer scheme is used for subgrid turbulent mixing (Boutle et al., 2014). With decreasing Δ more turbulence is resolved and the blending is increasingly weighted towards the local three-dimensional (3D) Smagorinsky–Lilly turbulence scheme (Halliwell, 2017; Lilly, 1962; Smagorinsky, 1963) rather than the nonlocal one-dimensional (1D) BL scheme (Lock et al., 2000). The land surface model is the Joint UK Land Environment Simulator (JULES: Best et al., 2011; Clark et al., 2011) and the module Met Office–Reading Urban Surface Exchange Scheme (MORUSES) treats the urban aspects of the surface (Bohnenstengel et al., 2011; Porson et al., 2010). MORUSES parametrises interactions between the urban surface and the atmosphere by assuming a 2D infinite street canyon geometry that accounts for the height and separation of buildings.

Analysis focuses on UKV, UM100, and UM55 because of scalar nonconservation issues in UM500 and UM300. At $\Delta = \mathcal{O}(500\ \text{m})$ the dominant CBL turbulence is in the "grey zone" (Honnert et al., 2020; Wyngaard, 2004), and updrafts become grid-scale. Also, SISL advection is not inherently conserving, meaning that, when wind is interpolated from grid points straddling a departure point in a single grid point updraft, there is cancellation of the wind, resulting in insufficient scalar dilution in the updraft, and excess scalar is produced (Blunn, 2021). The UKV, UM100, and UM55 passive scalar is much less influenced by passive scalar nonconservation issues, because the updrafts are not grid-scale in the mixed layer of the CBL. Also, the excess passive scalar produced in UM500 and UM300 does not influence the other models, because the passive scalar is not passed between model boundaries. There is ongoing work at the UK Met Office on ameliorating scalar nonconservation issues.

2.3 | Source and analysis regions

Two passive scalars are included in the simulations, one with continuous and the other with puff release from a ground-area source. The same source areas and emission rates are used in all models to facilitate comparison. The continuous-release passive scalar is from a homogeneous ground source with horizontal dimensions $(50 \times 50\ \text{km})^2$ (red dashed line, Figure 1b). The source provides a simple framework in which to study idealised city-scale spatial variation of passive scalar concentration over London. The puff-release passive scalar is also from a homogeneous ground source, but with its horizontal extent covering the entire UM100/UM55 domains (red solid line, Figure 1b). The puff releases are used to analyse vertical mixing timescales. Passive scalar is released on the hour and at the end of the hour it is completely flushed from the domain. An hour is long enough for the passive scalar to become well mixed in the CBL. The large source area enables an analysis region to be selected far enough in from the source boundaries that zero passive scalar air is not advected in within the hour.

Analysis region 1 (black dashed line, Figure 1b) starts 30 km downstream of the southern edge of the continuous source, extends 15 km downstream, and is 40 km in the cross-stream. It is large enough to contain > 10

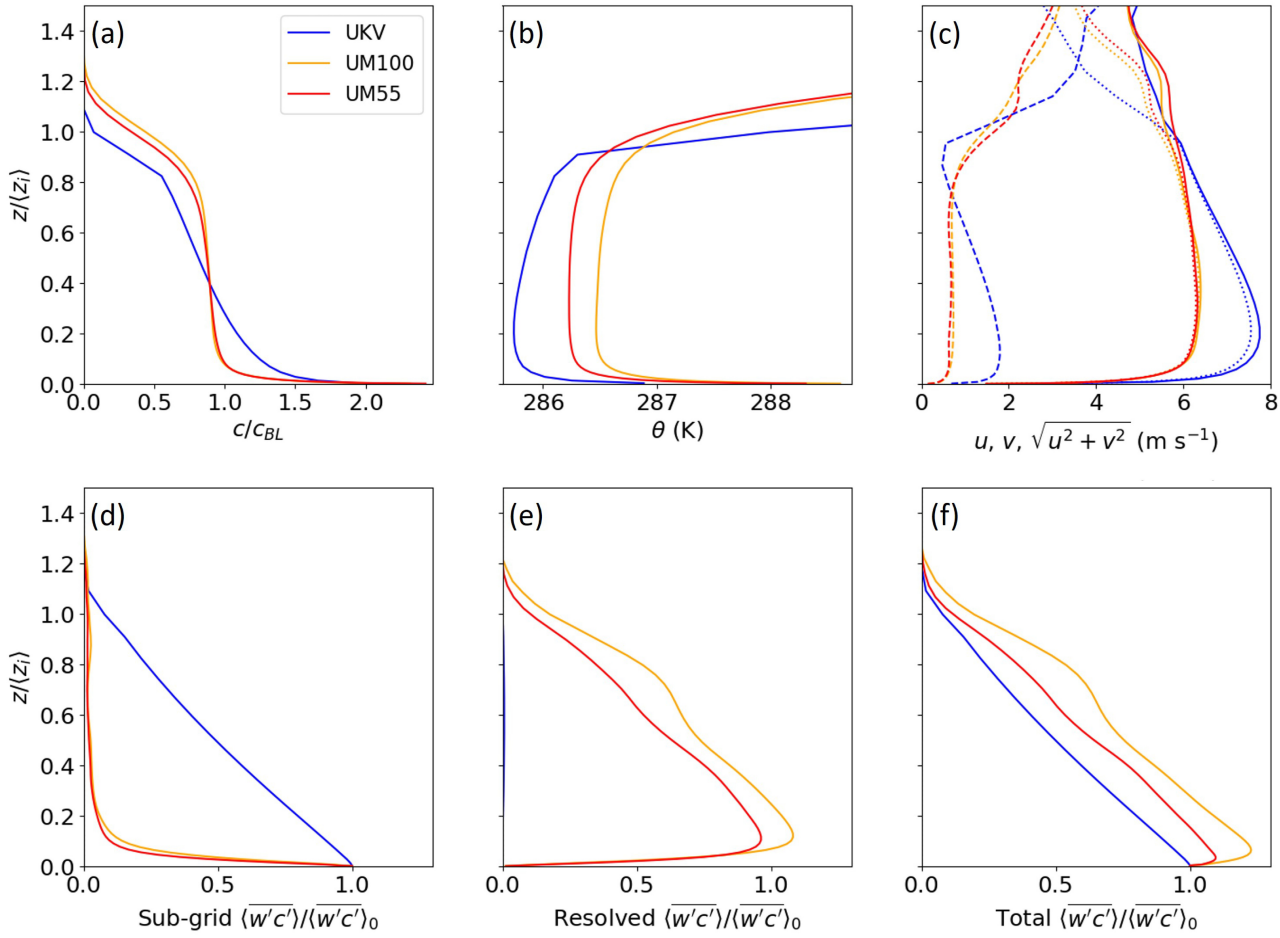

FIGURE 2 Horizontally averaged profiles in analysis region 1 at 1300 UTC: (a) continuous-release passive scalar concentration normalised by the average concentration in the BL, (b) potential temperature, (c) x-component of wind u (dashed line), y-component of wind v (dotted line), and wind speed (solid line), (d) subgrid passive scalar flux, (e) resolved passive scalar flux, and (f) total passive scalar flux. The y-axis is height above the ground normalised by the horizontally averaged boundary-layer height, which is 1608, 1475, and 1439 m for UKV, UM100, and UM55, respectively. [Colour figure can be viewed at wileyonlinelibrary.com]

CBL eddies (each with size of $\mathcal{O}(1\,\text{km})$), has minimal flow variation ($\sim 1\,\text{m s}^{-1}$, Figure 1b) on the scale of the analysis region, and has minimal z_i variation ($< 5\%$) on the scale of the analysis region. This ensures that flow statistics are robust and locally representative. Analysis region 2 (black solid line, Figure 1b) is used to study the evolution of the vertical passive scalar distribution with downstream distance from the upstream edge of the continuous-release source (Section 3.4).

3 | RESULTS AND DISCUSSION

3.1 | Convective boundary-layer structure

In this section, the vertical (Section 3.1.1) and horizontal (Section 3.1.2) structure of the CBL is analysed. Vertical profiles and vertical cross-sections provide information on the general structure of the CBL during the case study and insights into vertical mixing and passive scalar distribution differences between model resolutions. Passive scalar horizontal cross-sections and vertical velocity two-point correlations elucidate these differences further.

3.1.1 | Vertical structure

Vertical profiles of several variables are calculated within analysis region 1 (Figure 1b) at 1300 UTC for the continuous-release passive scalar and are plotted in Figure 2. Height from the ground z on the y-axis is normalised by $\langle z_i \rangle$, where z_i is the boundary-layer height, horizontally averaged $\langle\rangle$ within analysis region 1. Concentrations are normalised by the average concentration in the BL, c_{BL}. z_i is diagnosed by performing an adiabatic parcel ascent until the parcel becomes negatively buoyant.

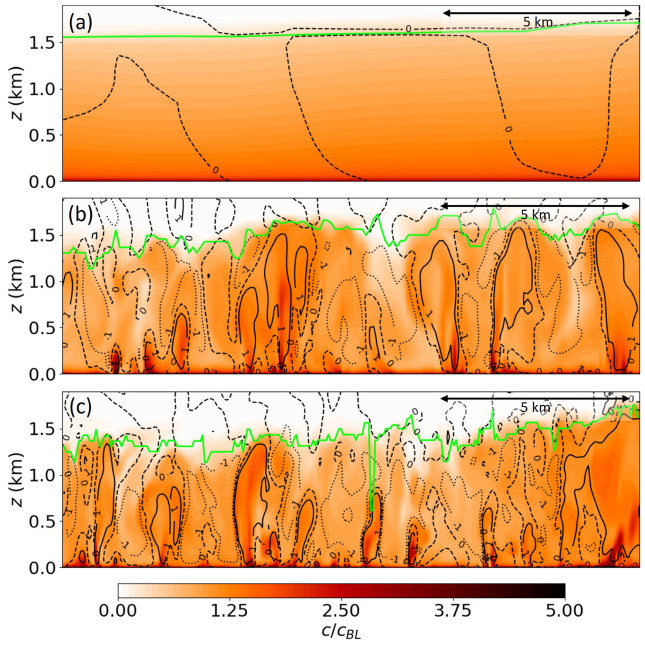

FIGURE 3 (a) UKV, (b) UM100, and (c) UM55 vertical cross-sections at 1300 UTC approximately perpendicular to the mean flow in the BL (see location in Figure 1b), showing continuous-release passive scalar concentration normalised by the average concentration in the BL. Black solid, dashed, and dotted lines are −1, 0, and 1 m s^{-1} vertical velocity contours, respectively. The lime solid line is BL scheme diagnosed z_i. [Colour figure can be viewed at wileyonlinelibrary.com]

The UM100 and UM55 passive scalar concentration c (Figure 2a) decreases sharply in the surface layer ($z/\langle z_i\rangle \approx$ 0.0–0.1) and is approximately constant in the mixed layer ($z/\langle z_i\rangle \approx$ 0.1–0.8), before decreasing through the capping inversion layer ($z/\langle z_i\rangle \approx$ 0.8–1.2) to zero. Similar behaviour can be seen for the UM100 and UM55 potential temperature θ in Figure 2b, except that θ increases in the capping inversion layer. The UM100 and UM55 passive scalar and potential temperature profiles exhibit classic CBL structure (Garratt, 1994; Pleim, 2007).

The UKV c (Figure 2a) and θ (Figure 2b) vary more strongly with height in the mixed layer compared with those for UM100/UM55. The capping inversion is narrower for UKV, and there is less passive scalar concentration above $\langle z_i\rangle$. This is because UM100 and UM55 have greater z_i heterogeneity due to updrafts and downdrafts. Also, resolved motions in UM100 and UM55 sometimes generate low-θ anomalies in the middle of the CBL, leading to erroneously low parcel ascent z_i diagnosis (see Figure 3c) and low θ and high c above z_i.

The UM100 and UM55 wind speeds are very similar (Figure 2c) and are ≈ 6 m s^{-1} for $z/\langle z_i\rangle \approx$ 0.1–1.2. The UKV wind speed has a maximum of 7.8 m s^{-1} at $z/\langle z_i\rangle \approx$ 0.2 and decreases to values (≈ 6 m s^{-1}) similar to UM100 and UM55 by $z/\langle z_i\rangle \approx 1.0$. The wind is predominantly from the south in all models, as expected based on measurements made at URAO (see Section 2.1). The UKV x-component of the wind (u) decreases more strongly with height and is ∼ 2 m s^{-1} larger than u in UM100 and UM55. Also, unlike UM100 and UM55, the UKV u has a distinct minimum in the capping inversion before increasing rapidly above.

The UKV subgrid (i.e., parameterised) (Figure 2d) and total (Figure 2f) turbulent passive scalar fluxes decrease linearly with height from the ground to $z/\langle z_i\rangle \approx 1.1$ where $c = 0$, as expected for a quasi-steady-state CBL (Wyngaard & Brost, 1984). The subgrid and total fluxes are equal to a very good approximation, because at $\mathcal{O}$(1 km) grid lengths turbulent transport is not resolved within the CBL, as seen for UKV in Figure 2e.

The UM100 and UM55 subgrid fluxes (Figure 2d) decrease rapidly in the surface layer (and slightly faster for UM55), before decreasing more gradually to zero where $c = 0$ at $z/\langle z_i\rangle \approx 1.2$. Above the surface layer, the UM100 and UM55 resolved fluxes (Figure 2e) dominate the total fluxes (Figure 2f). The total fluxes decrease approximately linearly in the range $z/\langle z_i\rangle \approx$ 0.1–1.2. Unlike UKV, UM100 (in particular) and UM55 have a small increase in total flux in the surface layer. This is likely due to nonconservation issues with grid-scale turbulence close to the surface (as discussed in Section 2.3). The subgrid/resolved flux partitioning for passive scalar here is consistent with that of Lean et al. (2019) for heat fluxes.

By considering the flux profiles and theory, it is possible to interpret the differences between the UKV and UM100/UM55 c and θ profile behaviour in the mixed layer. In the MetUM, the total vertical turbulent flux for a scalar variable χ is given by (Lock et al., 2016)

$$\overline{w'\chi'}_{\text{tot}} = \overline{w'\chi'}_{\text{res}} + \overline{w'\chi'}_{\text{sbg}}, \tag{1}$$

where $\overline{w'\chi'}_{\text{res}}$ is the resolved flux and $\overline{w'\chi'}_{\text{sbg}}$ is the subgrid flux given by

$$\overline{w'\chi'}_{\text{sbg}} = -\max\left[W_{1\text{D}}K_{\chi}^{\text{NL}}, K_{\chi}(\text{Ri})\right]\frac{\partial\chi}{\partial z} + W_{1\text{D}}K_{\chi}^{\text{NL}}\gamma_{\chi}. \tag{2}$$

The weighting function $W_{1\text{D}}$ controls the amount of subgrid flux mixing and is given by

$$W_{1\text{D}} = 1 - \tanh\left(0.15\frac{z_i}{\Delta}\right) \times \max\left\{0, \min\left[1, \frac{4}{15}\left(4 - \frac{\Delta}{z_i}\right)\right]\right\}. \tag{3}$$

It is a function of the dimensionless parameter Δ/z_i, and is designed to give the proportion of turbulent kinetic energy (TKE) that is resolved versus subgrid in LES at

various horizontal grid lengths (Boutle et al., 2014; Honnert et al., 2011). Between 1100 and 1400 UTC, the average weighting function values are 0.15, 0.95, and 1.00 for UKV, UM100, and UM55, respectively. This means that the mixed-layer turbulence is treated by UKV as 85% parametrised, and is 95% and 100% resolved in UM100 and UM55, respectively (i.e., to a good approximation, UM100 and UM55 are in LES mode). K_χ^{NL} is a nonlocal diffusivity, $K_\chi(\mathrm{Ri})$ is a local diffusivity, Ri is the local Richardson number, and γ_χ is a height-independent parameter determined by the surface and entrainment fluxes. In the surface layer, the local subgrid flux term begins to dominate the nonlocal subgrid flux terms (Equation 2), and towards the surface the turbulence becomes increasingly parameterised rather than resolved. The γ_χ term is a countergradient flux term that is independent of local gradients, and is included to make χ profiles more well mixed. However, it is only included when $\chi = \theta$. Specific humidity profiles tend to decrease in the upper CBL due to drying at the mixed-layer top, so for them the extra nonlocal term is not included (Lock et al., 2016). Passive scalars do not have their own tailored treatment in the MetUM, so have no countergradient term (Lock et al., 2016).

Given that the UKV θ profile (Figure 2b) increases more than expected in the mixed layer based on the CBL literature (Garratt, 1994; Pleim, 2007), and that UM100 and UM55 are more constant with height, it is likely that the countergradient term is not large enough to maintain a constant θ profile. Also, the absence of the countergradient term for c is likely why it decreases by approximately half in the mixed layer for UKV, but decreases by only $\approx 10\%$ for UM100 and UM55 where mixed-layer turbulence is almost all resolved.

Figure 3a–c shows vertical cross-sections approximately perpendicular to the mean flow of continuous-release passive scalar concentration for UKV, UM100, and UM55, respectively. The UKV field is smooth as expected, because the CBL turbulence is not resolved at $\mathcal{O}(1\,\mathrm{km})$ grid length. In UM100 and UM55, passive scalar converges near the surface into updrafts that are associated with high concentrations. The updrafts branch in the upper BL, due to the capping inversion forcing air to spread horizontally, before descending in downdrafts that are broader and have lower concentrations. Sometimes updrafts do not span the entire BL, which is expected because downdrafts act to suppress the less energetic updrafts beneath, and instantaneous fields can contain updrafts that have not had time to develop fully. The resolved motions in UM100 and UM55 are typical of those observed in idealised LES and experiments (Deardorff, 1972b; Willis & Deardorff, 1979). This is perhaps not surprising, considering that UM100 and UM55 are approximately in LES mode, but nonetheless it is important to demonstrate that CBL turbulence is well represented in hectometric NWP for realistic meteorology.

There is clearly more spatial detail in UM55 than UM100 concentration and vertical velocity fields. However, it is not immediately obvious whether the integral-scale turbulence (i.e., $\mathcal{O}(z_i)$ updrafts, downdrafts, and their spacing) is the same in UM100 and UM55. The convergence of UM100 and UM55 is examined in greater detail in Section 3.1.2.

3.1.2 | Horizontal structure

The nondimensional ratio $-z_i/L_\mathrm{O}$ with L_O the Obukhov length (Garratt, 1994) can be used to characterise the turbulent structure in CBLs (Salesky et al., 2017). We use values from our simulations to interpret whether the turbulence structure is as expected compared with the literature. Figure 4 shows horizontal cross-sections of continuous-release c and w for UM100 and UM55 at $z/\langle z_i\rangle = 0.1$, $z/\langle z_i\rangle = 0.5$, and $z/\langle z_i\rangle = 1.0$ at 1300 UTC. The ratio is approximately 28 and 30 for UM100 and UM55, respectively. UKV is not shown, since the fields are smooth (Figure 3). The UM100 and UM55 vertical velocity fields at $z/\langle z_i\rangle = 0.1$ (Figure 4a,b) are qualitatively similar to Figure 4 of Salesky et al. (2017), where the same field is shown, but generated using LES of a CBL with $-\langle z_i\rangle/L_\mathrm{O} = 26$. The turbulence, although elongated in the streamwise direction, retains some open cell-like structure typical of buoyancy-dominated CBLs ($-\langle z_i\rangle/L_\mathrm{O} \gg 20$). Salesky et al. (2017) showed that the largest changes in CBL structure occur around $-\langle z_i\rangle/L_\mathrm{O} = 15$–$20$, and for more shear-dominated conditions ($-\langle z_i\rangle/L_\mathrm{O} < 15$) horizontal convective rolls develop with little or no turbulent structure in the cross-stream.

The structure of the CBL can be understood further by inspecting the vertical velocity at $z/\langle z_i\rangle = 0.5$ (Figure 4e,f) and $z/\langle z_i\rangle = 0.1$ (Figure 4a,b). With increasing height the UM100 and UM55 updrafts become broader, updrafts and downdrafts are stronger, and less smaller scale turbulence is apparent. This is consistent with some updrafts not spanning the entirety of the CBL (Section 3.1.1) and the merging of smaller updrafts to form broader ones (Schmidt & Schumann, 1989). At $z/\langle z_i\rangle = 1.0$ (Figure 4i,j) the updrafts reach the capping inversion, where they spread horizontally into domes, becoming less aligned with the flow.

It is clear from the c horizontal cross-sections in Figure 4 that c correlates strongly with w. The standard deviation of c normalised by the average concentration in the layer ($\langle c\rangle$) is calculated at $z/\langle z_i\rangle = 0.1$ at 1300 UTC in analysis region 1 (Figure 1b). For both UM100 and UM55 the value is 0.32. Assuming a Gaussian distribution, one would expect 2.1% of values to be greater than the mean

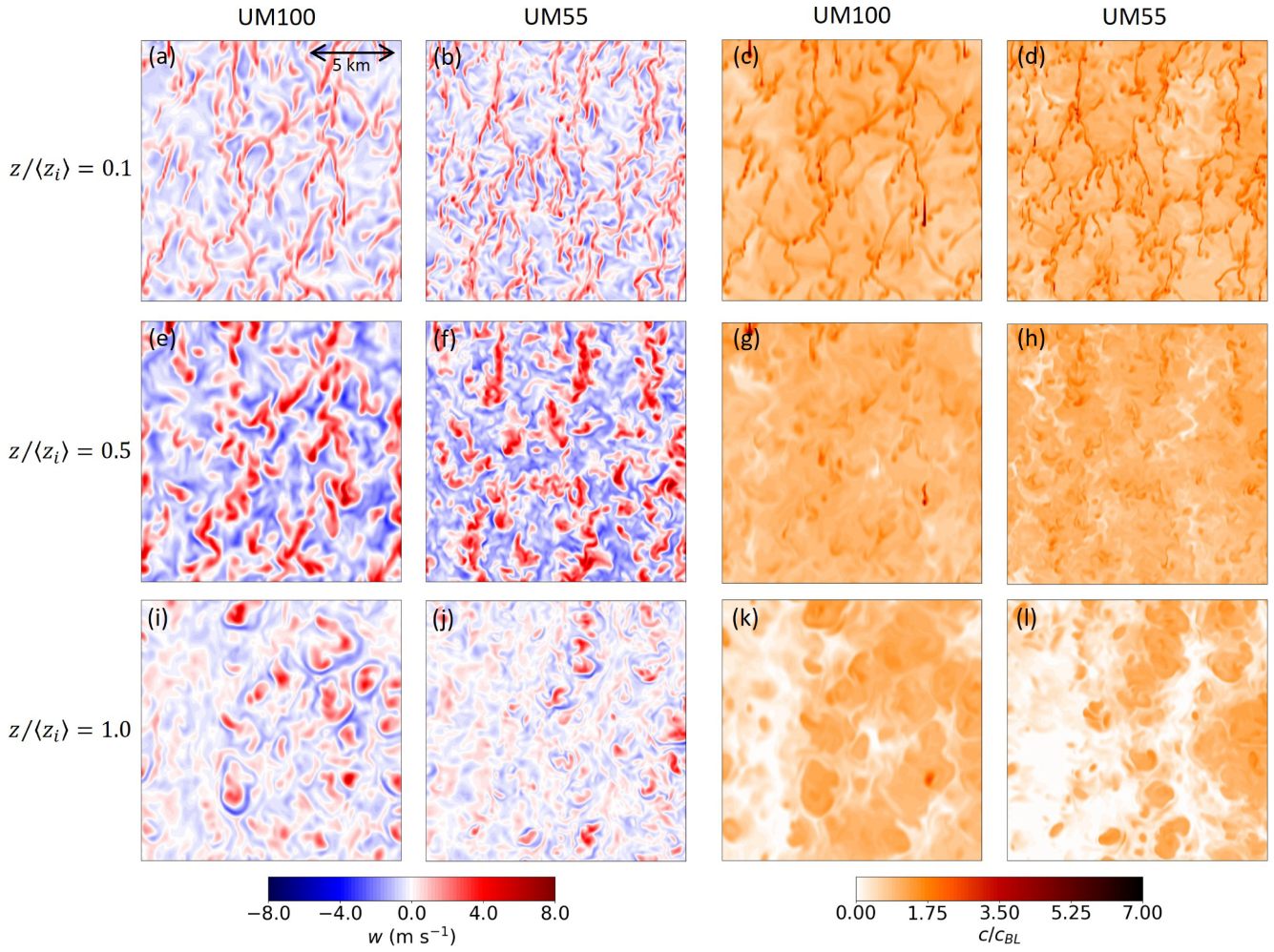

FIGURE 4 Horizontal cross-sections of (a,b,e,f,i,j) vertical velocity (columns 1 and 2) and (c,d,g,h,k,l) continuous-release passive scalar concentration normalised by the average concentration in the BL (columns 3 and 4), for (a,b,c,d) $z/\langle z_i\rangle = 0.1$ (row 1), (e,f,g,h) $z/\langle z_i\rangle = 0.5$ (row 2), and (i,j,k,l) $z/\langle z_i\rangle = 1.0$ (row 3). The UM55 columns are (a,e,i) 1 and (c,g,k) 3, and the UM100 columns are (b,f,j) 2 and (d,h,l) 4. See Figure 1b for location. [Colour figure can be viewed at wileyonlinelibrary.com]

plus twice the standard deviation ($= 1.64\langle c\rangle$). However, the distribution exhibits positive skewness, with approximately 5% of values greater than $1.64\langle c\rangle$, making large values of c more likely compared with a Gaussian distribution. It is perhaps surprising that, 30–45 km downstream of the southern edge of the homogeneous continuous-release source, c is often considerably larger than its mean value. Passive scalar emitted near the southern edge of the source region has time to become well mixed 30–45 km downstream, yet it does not totally dominate the near-surface passive scalar concentration. This is because local emissions that converge into updrafts can still lead to considerable horizontal heterogeneity. This raises the question of whether convergence at the base of updrafts causes significant transient surface-level pollution concentration heterogeneity in cities. Investigation would need to account for building-scale turbulence, so experimental methods or building-resolving LES would be suitable.

We note that in the UM100 horizontal cross-sections there is some evidence of grey-zone issues. Grid-scale updrafts align with the grid at $z/\langle z_i\rangle = 0.1$ (Figure 4a,c), causing large c and w throughout the CBL (Figure 4e,g,i,k) (Blunn, 2021, their Figure 3.15).

There is more detailed turbulent structure in UM55 than in UM100 (Figure 4), but, as in Section 3.1.1, it is not clear whether the integral-scale $\mathcal{O}(z_i)$ CBL eddies are resolved fully by UM100. While we do not assume that UM55 resolves the integral-scale turbulence fully, it can be used as a reference for UM100, to test convergence with decreasing Δ. Convergence is investigated using the two-point cross-correlation function, which for two variables χ_1 and χ_2 at height z is given by

$$R_{\chi_1\chi_2}(L) = \frac{<(\chi_1(l) - \langle\chi_1\rangle)(\chi_2(l') - \langle\chi_2\rangle)>}{<(\chi_1(l) - \langle\chi_1\rangle)(\chi_2(l) - \langle\chi_2\rangle)>}, \qquad (4)$$

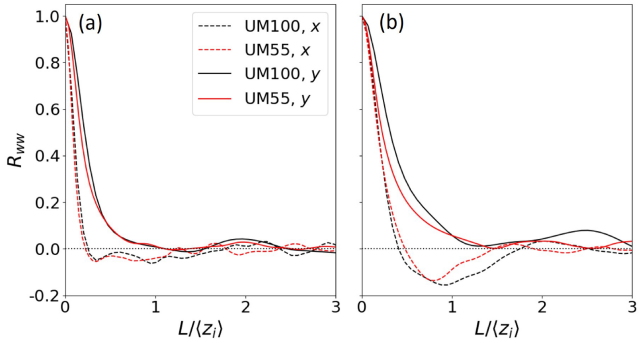

FIGURE 5 Vertical velocity two-point cross-correlation functions plotted against $L/\langle z_i \rangle$ at 1300 UTC for (a) $z/\langle z_i \rangle = 0.1$ and (b) $z/\langle z_i \rangle = 0.5$. Black and red lines correspond to UM100 and UM55, respectively, and dashed and solid lines correspond to cross-correlations along the x- and y-axes, respectively. [Colour figure can be viewed at wileyonlinelibrary.com]

where $L \equiv l - l'$ is the spatial separation between l and another point l', and $\langle\rangle$ is the horizontal spatial average. When calculating R_{ww} for $l = x$ (i.e., R^x_{ww} cross-correlations along the east–west axis), the cross-correlation is calculated at each y, then averaged, and vice versa for $l = y$ (i.e., R^y_{ww} cross-correlations along the north–south axis). The term "turbulence integral length scale" will be used to mean any length scale that characterises the largest turbulence scale. This includes updraft width and separation and statistical measures.

In Figure 5 we plot R_{ww} for UM100 and UM55 in analysis region 1 at 1300 UTC, for $z/\langle z_i \rangle = 0.1$ and $z/\langle z_i \rangle = 0.5$, with $l = x$ and $l = y$. The first R^x_{ww} zero-crossing corresponds to the typical updraft width. Values are calculated at 1100, 1200, 1300, and 1400 UTC, and the averages and standard deviations (σ) (calculated over the four times) for UM100 and UM55 are given in Table 2. The four times are chosen because the CBL was fairly consistent then (with $-\langle z_i \rangle / L_O = 29.3 \pm 2.6$ and $-\langle z_i \rangle / L_O = 29.8 \pm 2.1$ for UM100 and UM55, respectively), and to enable the differences in R_{ww} characteristics between the two models to be compared with consideration of the statistical uncertainty associated with using instantaneous snapshots. At $z/\langle z_i \rangle = 0.1$, the first R^x_{ww} zero-crossing is $(0.235 \pm 0.006)\langle z_i \rangle$ and $(0.208 \pm 0.005)\langle z_i \rangle$, for UM100 and UM55, respectively. The zero crossings at $z/\langle z_i \rangle = 0.5$ are $(0.419 \pm 0.026)\langle z_i \rangle$ and $(0.446 \pm 0.044)\langle z_i \rangle$, for UM100 and UM55, respectively. Updrafts in both models are approximately twice as wide at $z/\langle z_i \rangle = 0.5$ compared with $z/\langle z_i \rangle = 0.1$.

For L greater than the first R^x_{ww} zero-crossing and smaller than the second R^x_{ww} zero-crossing, there is a minimum where the updrafts are anticorrelated with the downdrafts. The second R^x_{ww} zero-crossing corresponds to where the updrafts come back in phase, and therefore represents the cross-stream updraft separation. Its values are given in Table 2. In both models the cross-stream updraft separation increases only slightly from $\approx 1.5\langle z_i \rangle$ to $\approx 1.74\langle z_i \rangle$ between $z/\langle z_i \rangle = 0.1$ and $z/\langle z_i \rangle = 0.5$. The updraft width increases more strongly with height than the cross-stream updraft separation. The updraft width to cross-stream updraft separation ratio is approximately 0.15 and 0.25 at $z/\langle z_i \rangle = 0.1$ and $z/\langle z_i \rangle = 0.5$, respectively, for both UM100 and UM55.

The updrafts are generally aligned in the streamwise direction, have finite streamwise length, and meander in the cross-stream direction. As the w fields are increasingly separated, the updrafts eventually become uncorrelated, with the streamwise cross-correlations, R^y_{ww}, having no prominent negative minima, since there is little streamwise repetitive turbulence structure. Therefore, zero-crossings cannot be used to define the turbulence integral length scale. A common alternative method for calculating the turbulence integral scale is to integrate the two-point cross-correlation function $\int_0^\infty R_{ww} dL$ (Dosio et al., 2005). Here we take the upper integral limit to be the separation at which $R^y_{ww} < 0.1$ ($L_{0.1}$), so that any large-scale structures ($L \gg \mathcal{O}(z_i)$) in the w field unrelated to turbulence are not included.

The streamwise turbulence integral length scale $\int_0^{L_{0.1}} R^y_{ww} dL$ at $z/\langle z_i \rangle = 0.1$ is $(0.257 \pm 0.016)\langle z_i \rangle$ and $(0.213 \pm 0.009)\langle z_i \rangle$ for UM100 and UM55, respectively, where the averages and standard deviations are over times 1100, 1200, 1300, and 1400 UTC. The values are $> 2\sigma$ from

TABLE 2 The average and standard deviation of the turbulence integral length scale values for UM100 and UM55 calculated at $z/\langle z_i \rangle = 0.1$ and $z/\langle z_i \rangle = 0.5$ from R^x_{ww} and R^y_{ww}.

	$z/\langle z_i \rangle = 0.1$		$z/\langle z_i \rangle = 0.5$	
Turbulence integral length scale	**UM100**	**UM55**	**UM100**	**UM55**
First R^x_{ww} zero-crossing	0.235±0.006	0.208±0.005	0.419±0.026	0.446±0.044
Second R^x_{ww} zero-crossing	1.446±0.274	1.544±0.300	1.711±0.281	1.767±0.254
$\int_0^{L_{0.1}} R^y_{ww} dL$	0.257±0.016	0.213±0.009	0.371±0.025	0.359±0.070

Note: The average and standard deviation are calculated from values at 1100, 1200, 1300, and 1400 UTC. The unit of all length scales is $\langle z_i \rangle$.

each other, suggesting that the UM55 streamwise turbulence integral length scale is generally smaller than that of UM100. The streamwise turbulence integral length scale at $z/\langle z_i \rangle = 0.5$ is $(0.371 \pm 0.025)\langle z_i \rangle$ and $(0.359 \pm 0.070)\langle z_i \rangle$ for UM100 and UM55, respectively. Again, the UM55 streamwise turbulence integral length scale is slightly smaller than the UM100 one, but they are within σ of one another, so this could be due to statistical variation in time.

The first R^x_{ww} zero-crossing is $> 3\sigma$ smaller for UM55 than for UM100 at $z/\langle z_i \rangle = 0.1$. However, the UM100 and UM55 values are within σ of each other for the first R^x_{ww} zero-crossing at $z/\langle z_i \rangle = 0.5$ and the second R^x_{ww} zero-crossings at $z/\langle z_i \rangle = 0.1$ and $z/\langle z_i \rangle = 0.5$.

For the R^x_{ww} first zero-crossing at $z/\langle z_i \rangle = 0.1$ and R^y_{ww} integral length scale at $z/\langle z_i \rangle = 0.1$, where mean values are $> 3\sigma$ and $> 2\sigma$ away from each other, respectively, the UM55 turbulence scales are smaller than those for UM100. This suggests that, near the top of the surface layer (often considered to be $z/\langle z_i \rangle \approx 0.1$), the UM100 integral-scale turbulence has not converged. However, in the middle of the CBL, where smaller scale turbulence associated with the surface layer has merged into larger updrafts spanning the CBL, UM100 demonstrates signs of convergence.

Lean et al. (2022) conducted 100-, 55-, and 25-m Δ MetUM simulations for a clear-sky day with $z_i \approx 750$ m. At $z/z_i = 0.4$ they found no signs of updraft width convergence. This is consistent with the behaviour at $z/\langle z_i \rangle = 0.1$ rather than $z/\langle z_i \rangle = 0.5$ in our study. This could be due in part to updrafts at $z/z_i = 0.4$ being nearer the surface and therefore narrower than at $z/z_i = 0.5$, but more likely it is because z_i is approximately a factor of two smaller in the Lean et al. (2022) simulations, so that the turbulence is smaller scale and updrafts are narrower. From power spectra at $z/z_i = 0.25$, at energy-producing scales Lean et al. (2019) found modelled turbulence to be most similar to observed turbulence for $\Delta = 25$ m. This suggests that, to represent the integral-scale turbulence in the lower portion of the CBL fully, at least $\Delta = 25$ m is required. However, for deep CBLs ($\mathcal{O}(z_i = 1.4\,\text{km})$), particularly towards the middle of the CBL, our study suggests that some integral-scale properties of the turbulence (e.g., cross-stream updraft separation) start to show signs of convergence at $\Delta = 100$ m.

3.2 | Vertical evolution following puff release

In this section, the evolution of the vertical profile of the passive scalar field is investigated for UKV, UM100, and UM55. A qualitative investigation is made using vertical cross-sections and vertical profiles of the puff-release passive scalar concentrations. Timescales associated with the vertical mixing in each model are investigated in Section 3.3.

Figure 6 shows vertical cross-sections of (a–c) UKV and (d–f) UM55 1300 UTC puff-release passive scalar at 5, 20, and 55 min since release. The cross-sections are approximately perpendicular to the flow (see location in Figure 1b). At 1305 UTC, the UKV passive scalar concentration is very horizontally homogeneous and high near to the surface, but the UM55 concentration is much more horizontally and vertically heterogeneous, with high concentration values at greater heights than for UKV. These high values can be found up to $z = 1$ km and are associated with updrafts resolved in UM55. At 1320 UTC, the UKV concentration is still higher near the surface and lower near the top of the BL, but the vertical gradient is reduced. At the same time, there is more passive scalar in the upper BL than lower BL for UM55. Therefore, the lift-off behaviour seen in experiments and LES is demonstrated here (Deardorff, 1972b; Willis & Deardorff, 1976). By 1355 UTC, the UKV concentration field is very homogeneous throughout the BL. The UM55 concentration field has become much more homogeneous, but vertical and horizontal structure still remains.

Differences in the vertical evolution of passive scalar concentration between models can be further understood by inspecting vertical profiles. Figure 7 shows the 1300 UTC puff-release concentration profiles for UKV, UM100, and UM55 in analysis region 1 (Figure 1b) at 5-min intervals. The UKV concentration profiles decrease and increase monotonically with time near the surface and in the upper BL, respectively, and tend towards a steady state. The UKV concentration decreases monotonically with height at all times. The UM100 and UM55 profiles are most similar to the UKV profile at 5 min, which is likely due to vertical mixing near the surface being partly parameterised in all models. However, after 10 min UM100 and UM55 have a much larger proportion of passive scalar in the upper BL than UKV. Between approximately 15 and 30 min, UM100 and UM55 have more passive scalar in the upper BL than the lower BL. The surface-level concentrations 20 min after release are approximately three times lower for UM55 than for UKV. The lofting of passive scalar emitted at the surface is thus an important process controlling surface-level pollution concentration.

By 1340 UTC, the UM100 and UM55 profiles change very little with time and decrease by less than 20% between the surface and $z/\langle z_i \rangle = 0.8$ (i.e., are "well mixed"), despite the passive scalar heterogeneity seen in Figure 6f. The UM100 and UM55 profiles are very similar across times, demonstrating that the lower resolution UM100 represents

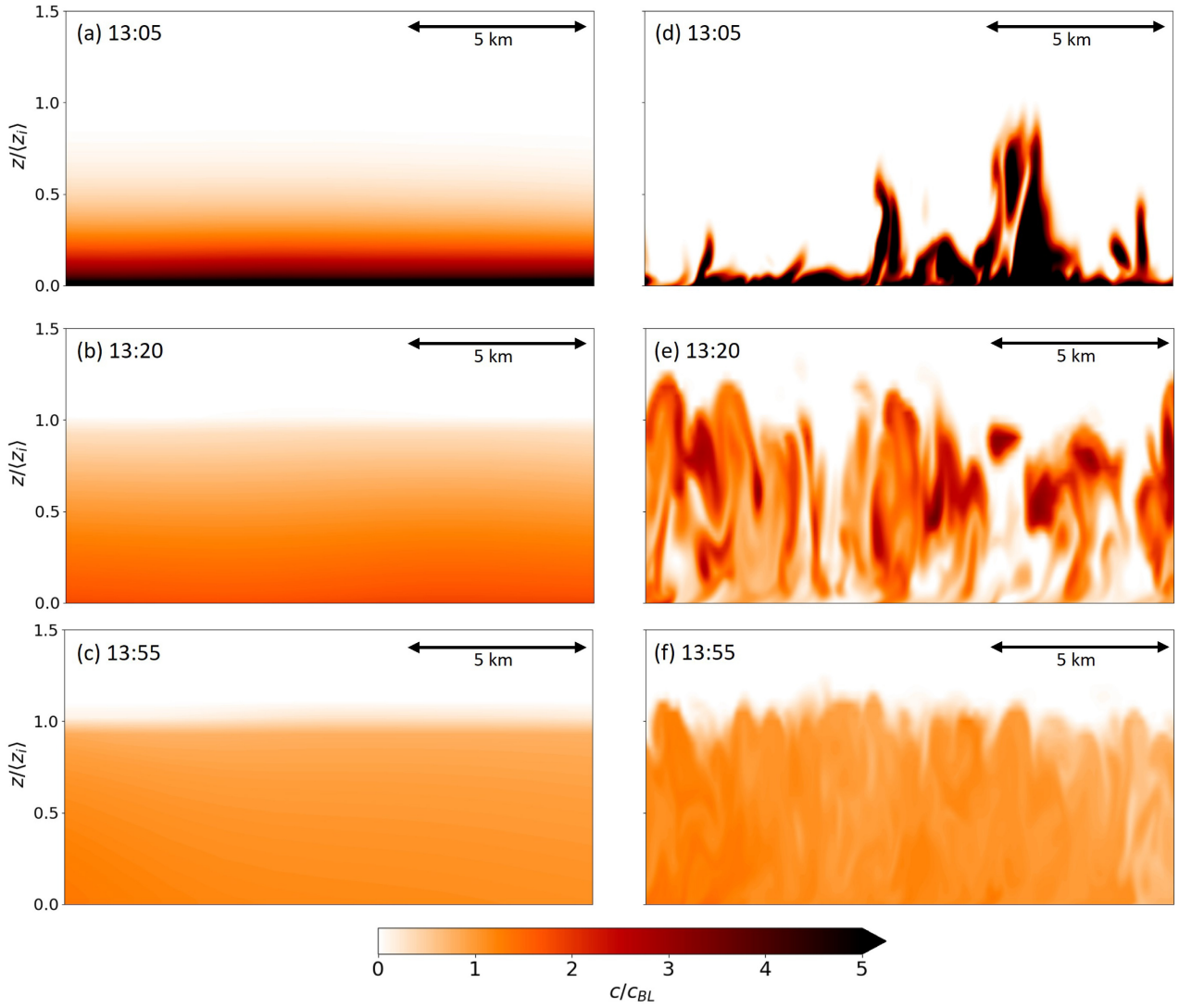

FIGURE 6 Vertical cross-sections approximately parallel to the mean flow in the BL (location Figure 1b) showing puff-release passive scalar concentration normalised by the average concentration in the BL. (a,b,c) UKV at 1305, 1320, and 1355 UTC, respectively, and (d,e,f) UM55 at 1305, 1320, and 1355 UTC, respectively. [Colour figure can be viewed at wileyonlinelibrary.com]

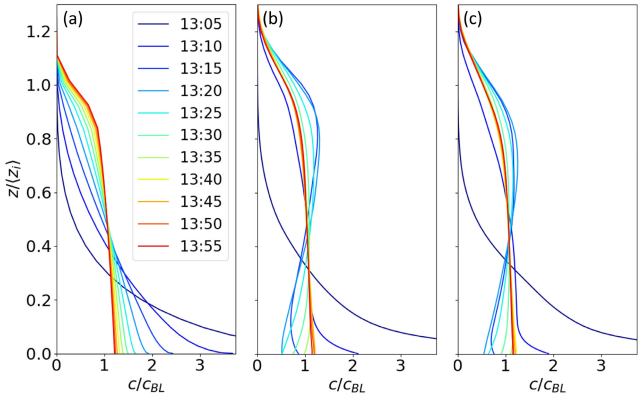

FIGURE 7 Time evolution of the 1300 UTC puff-release concentration profiles for (a) UKV, (b) UM100, and (c) UM55 models. Profiles are calculated in analysis region 1 (see location in Figure 1b). [Colour figure can be viewed at wileyonlinelibrary.com]

the most important passive scalar CBL turbulent mixing processes.

3.3 | Dispersion timescales

It was seen in previous sections that UKV and UM100/UM55 have different vertical mixing behaviour, and that passive scalar is mixed more efficiently in UM100/UM55 (e.g., Figure 2a). Here, a reduced analytical model is developed that enables the vertical mixing characteristics exhibited by the models to be attributed to different dispersion processes (i.e., diffusive and ballistic). Vertical mixing timescales associated with the processes are derived by fitting the reduced analytical model to the NWP output. The differences in vertical mixing behaviour between models are thus quantified.

The height of passive scalar may be characterised by the centre of mass:

$$\mathrm{CoM} = \frac{\int_A \int_0^\infty c(x,y,z) z \, dz \, dA}{\int_A \int_0^\infty c(x,y,z) \, dz \, dA}, \tag{5}$$

where A is the area of the analysis region (taken here to be analysis region 1). By tracking the CoM trajectory with time, one can obtain an estimate of how well mixed the passive scalar is, since, assuming that the amount of passive scalar that escapes the BL is negligible, $\mathrm{CoM}/\langle z_i \rangle \rightarrow 0.5$ in the limit of being well mixed.

The Lagrangian stochastic modelling approach is based on calculating an ensemble of particle trajectories through a turbulent flow, given knowledge of Eulerian velocity statistics. The ensemble average of such trajectories defines the concentration distribution. The mathematical form of most LSMs is that of the generalised Langevin equation (Thomson & Wilson, 2012). Importantly, it has the correct dispersion behaviour in the ballistic ($t \ll \tau$) and diffusive ($t \gg \tau$) limits.

As argued in the Appendix A, if various simplifying assumptions about CBL turbulence hold, then the evolution of the CoM can be roughly approximated by

$$\ddot{\tilde{Z}} = -2\gamma \dot{\tilde{Z}} - \omega^2 \tilde{Z}, \tag{6}$$

where $\tilde{Z} \equiv \tilde{z} - \langle z_i \rangle / 2$, $\tilde{z}$ is the ensemble average (tilde) height of a LSM's passive scalar particles and is equivalent to the CoM, $\omega = 2\pi/\tau_\omega$ is the natural frequency (which is related to the eddy turnover timescale), and $\gamma = 1/(2\tau)$ determines the amount of damping. This is the form of a damped simple harmonic oscillator (DSHO). The first "damping" term on the right-hand side represents the diffusive dispersion caused by smaller eddies, which cause particles to lose memory of the CBL-spanning eddy into which each particle was initially released. The second term on the right-hand side is an approximation to the LSM drift term (see Appendix A), which offsets the tendency of particles to accumulate in areas of low vertical velocity variance and is related to turbulent motions induced by pressure gradients in the CBL, that is, $\mathcal{O}(z_i)$ overturning eddies (Thomson, 1987).

The general solution to Equation 6 is given by

$$\tilde{Z}/\langle z_i \rangle = Ae^{p_+ t} + Be^{p_- t} = e^{-\gamma t}\left(Ae^{\sqrt{\gamma^2-\omega^2}\,t} + Be^{-\sqrt{\gamma^2-\omega^2}\,t}\right), \tag{7}$$

where A and B are dimensionless constants and $p_\pm = -\gamma \pm \sqrt{\gamma^2 - \omega^2}$. We can consider two regimes: overdamped ($\gamma > \omega$) and underdamped ($\gamma < \omega$), where dispersion is diffusive and ballistic-dominated, respectively. In the diffusive limit ($\gamma \gg \omega$) $p_+ \rightarrow 0$ and $p_- \rightarrow -2\gamma$, so that there is effectively one decay term in Equation 7. We define two timescales $\tau_{p_\pm} = -1/p_\pm$, such that in the diffusive limit $\tau_{p_+} \rightarrow \infty$ and $\tau_{p_-} \rightarrow 1/(2\gamma) = \tau$. τ is a memory timescale characterising how long it takes the motion of a particle to become uncorrelated with the motion of the particle immediately after release (see Appendix A).

For a ground release $\tilde{z}(0)/\langle z_i \rangle = 0$, it follows from Equation 7 that $A + B + 0.5 = 0$. The overdamped case of Equation 7 can then be written as

$$\tilde{z}/\langle z_i \rangle = 0.5 + Ae^{p_+ t} - (0.5 + A)e^{p_- t}, \tag{8}$$

where $p_+, p_- < 0$, and the underdamped case can be written as

$$\tilde{z}/\langle z_i \rangle = 0.5\left[1 - \frac{e^{-\gamma t}\cos(\Omega t + \phi)}{\cos(\phi)}\right], \tag{9}$$

where ϕ is a phase constant and $\Omega = \sqrt{\omega^2 - \gamma^2}$. Both solutions have two effective time parameters: $\tau_{p_-} = -1/p_-$ and $\tau_{p_+} = -1/p_+$ (overdamped), and $\tau = 1/(2\gamma)$ and $\tau_\Omega = 2\pi/\Omega$ (underdamped). A critically damped solution occurs when $\gamma = \omega$, and is given by

$$\tilde{z}/\langle z_i \rangle = 0.5 + (-0.5 + Jt)e^{-\gamma t}, \tag{10}$$

where J is a constant.

The overerdamped solution (Equation 8) decays exponentially with two timescales towards $\tilde{z}/\langle z_i \rangle = 0.5$ without oscillating. When ω is only slightly smaller than γ, then the two timescales $\tau_{p_\pm}$ in the exponential terms are both approximately equal to 2τ. As ω becomes increasingly smaller than γ, τ_{p_+} becomes larger than τ_{p_-}, until, as discussed previously, in the diffusive limit $\tau_{p_+} \rightarrow \infty$ and $\tau_{p_-} \rightarrow \tau$. The underdamped solution (Equation 9) oscillates at frequency Ω (slower than ω) with amplitude exponentially decaying to zero with e-folding lifetime $1/\gamma = 2\tau$, so that $\tilde{z}/\langle z_i \rangle$ tends towards 0.5. For a near-ground release, increasing ω results in $\tilde{z}$ moving more quickly from the surface, since the oscillations are faster. Also, as ω becomes larger relative to γ (i.e., increasingly ballistic-dominated dispersion), the oscillations are more prominent and $\tilde{z}/\langle z_i \rangle$ overshoots 0.5 more, since the solution has undergone less decay by the time of maximum amplitude.

The optimal fits between Equations 8 and 9 and the UKV, UM100, and UM55 puff-release $\tilde{z}$ time series are found by varying the parameter values and minimising the root-mean-square error. Figure 8 shows these time series and the fitted analytical solutions for a puff release at 1300 UTC. The solutions reproduce the salient features of the simulation results. UKV is fitted best by the overdamped solution, and $\tilde{z}/\langle z_i \rangle$ tends increasingly slowly with time towards 0.5. UM100 and UM55 are fitted best by the underdamped solution, where $\tilde{z}/\langle z_i \rangle$ increases rapidly and overshoots $z/\langle z_i \rangle = 0.5$ after $\approx$ 15 min, before settling at $\approx$

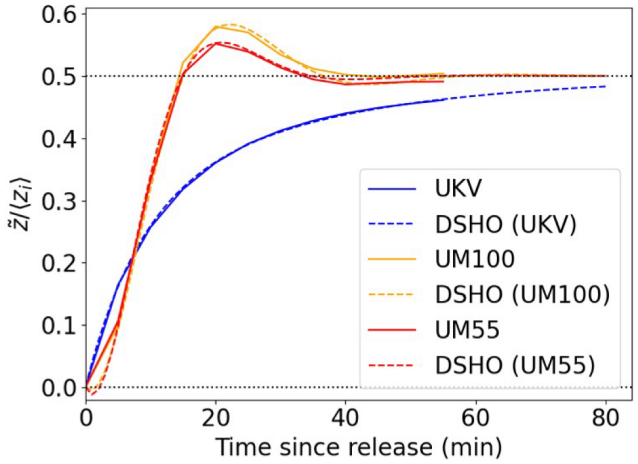

FIGURE 8 UKV, UM100, and UM55 model CoM trajectories for a puff release at 1300 UTC (solid) with optimal DSHO solutions (dashed). The trajectories and optimal solutions are also qualitatively representative of releases at 1100, 1200, and 1400 UTC. [Colour figure can be viewed at wileyonlinelibrary.com]

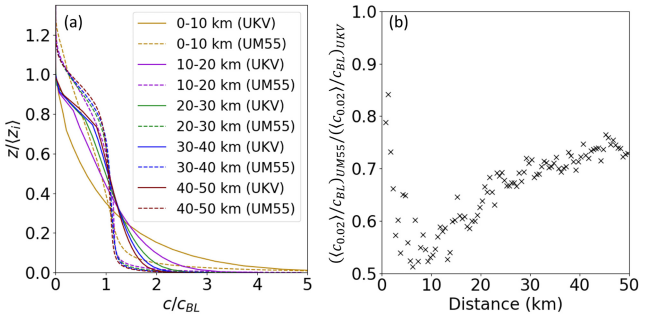

FIGURE 9 (a) UKV and UM55 continuous-release passive scalar concentration profiles normalised by the average concentration in the BL at 1300 UTC. Concentrations are calculated in five west–east bands across analysis region 2 (see location in Figure 1b): 0–10, 10–20, 20–30, 30–40, and 40–50 km downstream of the southern edge of the source. (b) Ratio of the UM55 to UKV continuous-release passive scalar concentration at $z/\langle z_i \rangle = 0.02$ normalised by the average concentration in the BL at 1300 UTC. The ratio is calculated in analysis region 2 at 0.5-km intervals downstream of the southern edge of the source. [Colour figure can be viewed at wileyonlinelibrary.com]

0.5. Also, the eddy turnover timescale $\tau_w = 105.2$ min is much slower than the decorrelation timescale $\tau = 6.7$ min, consistent with the lack of ballistic-type dispersion in UKV.

The best-fitting parameter values for puff releases at 1100, 1200, 1300, and 1400 UTC are calculated, and their average values are given in Table 3. These times are selected as they are highly convective and the CBL is quasi-stationary with $1.4 < z_i < 1.6$ km across all models. For UKV, τ_{p_-} and τ_{p_+} are 8.4 and 33.6 min, respectively. The τ_{p_-} term in Equation 8 decays quickly and largely determines the short-timescale dispersion behaviour. The τ_{p_+} term decays more slowly and largely determines the time it takes for passive scalar to become well mixed.

For UM55, τ and τ_ω are 4.6 and 33.3 min, respectively, and for UM100 τ and τ_ω are 5.7 and 36.0 min, respectively. This means that the resolved overturning motions associated with ballistic dispersion have a short enough timescale ($\tau_\omega < 4\pi\tau$, i.e., underdamped $\gamma < \omega$) to cause the CoM to overshoot $\langle z_i \rangle/2$ (see Figure 8), so that more passive scalar is in the upper than the lower half of the CBL. The τ decay term in Equation 9controls how quickly $\tilde{z}/\langle z_i \rangle$ reaches a steady-state value of 0.5 (i.e., becomes well mixed). Thus the timescale that determines how quickly the models become well mixed is $\tau_{p_+}/(2\tau) \approx$ three times longer for UKV than for UM100/UM55, consistent with the UKV vertical mixing being less efficient in Section 3.1.1. UM55 having slightly smaller τ and τ_Ω than UM100 is consistent across times (not shown), suggesting that the UM100 and UM55 vertical mixing has small differences and has not converged at $\Delta = 100$ m.

The convective timescale $t_* = \langle z_i \rangle / w_*$, where w_* is the convective velocity scale (Garratt, 1994), is 11.9 and 11.6 min for UM100 and UM55, respectively. Its value is $t_* \approx 2\tau$ in the UKV overdamped solution, while $t_* \sim \tau_\omega/3$ for the underdamped cases.

At very short times (0–5 min), the vertical mixing is slightly more efficient in UKV than in UM100/UM55 (Figure 8). This is possibly due to the vertical grid length being ~ two times larger in UKV compared with UM100/UM55, influencing parameterised vertical mixing near the surface. The best-fitting UM100/UM55 solutions have $\phi = -44°$ on average. This results in $\tilde{z}/\langle z_i \rangle$ becoming negative for a very short time, before becoming positive and increasing rapidly. This unphysical behaviour is a limitation of the model. That the optimal fit has $\phi \neq 0$ is likely a consequence of assuming that turbulence is vertically homogeneous in the first and third terms on the right-hand side of Equation A3.

3.4 | City-scale near-surface concentration dependence on vertical mixing

It was demonstrated in Sections 3.2 and 3.3 that, unlike passive scalar in UKV, passive scalar in UM100 and UM55 has higher concentrations in the upper half of the CBL at times $\approx \tau_\Omega/2$ since puff release (i.e., half the time period of the underdamped DSHO). This is due to UM100 and UM55 representing the lift-off behaviour that occurs in the ballistic dispersion limit. In this section, we investigate the influence of representing (UM100 and UM55) versus not representing (UKV) the lift-off effect on passive scalar

TABLE 3 Average optimal-fit DSHO parameter values for the UKV, UM100, and UM55 CoM trajectories.

Model	A	ϕ	τ_{p_+}	τ_{p_-}	τ	τ_Ω	τ_ω	t_*
UKV	−0.21	—	33.6	8.4	6.7	—	105.2	11.9
UM100	—	−38°	—	—	5.7	41.8	36.0	11.9
UM55	—	−44°	—	—	4.6	40.8	33.3	11.6

Note: The average is over the values at 1100, 1200, 1300, and 1400 UTC. $\tau_{p_+} = -1/p_+$, $\tau_{p_-} = -1/p_-$, $\tau_\Omega = 2\pi/\Omega$, $\tau = 1/(2\gamma)$, and $\tau_\omega = 2\pi/\omega$. $B = -A - 0.5$. Also included is the convective timescale $t_* = \langle z_i \rangle / w_*$. The unit of all timescales is minutes.

vertical distribution evolution with downstream distance over London. A homogeneous continuous ground source of passive scalar represents idealised city-scale pollution emissions. Figure 9a shows the UKV and UM55 profiles normalised by the mean concentration within the BL at 1300 UTC. The profiles are calculated in five west–east bands across analysis region 2 (see location in Figure 1b) at 0–10, 10–20, 20–30, 30–40, and 40–50 km downstream distance from the southern edge of the source.

The downstream distance (D) at which the profiles become steady state can be used to understand the efficiency of vertical mixing. Profiles become steady state when the majority of passive scalar is well mixed, which occurs at smaller D with increasing vertical mixing efficiency. For all models, immediately downstream of the source edge the passive scalar is near the surface, and, with increasing D, more of the passive scalar has time to become well mixed. The UKV profiles tend towards (but do not reach) a steady state with increasing D. The UM55 profiles change with D more quickly and reach an approximate steady state by the 10–20 km profile. The UKV vertical mixing is less efficient than that in UM55 (as discussed in Section 3.3) so the profiles take longer to adjust. Unlike the UM55 puff-release passive scalar profiles (see Figure 7c), due to the continuous ground-source emissions of passive scalar, there is never more UM55 passive scalar in the upper CBL than the lower CBL (Figure 9a). However, ballistic-regime turbulent mixing is still occurring, as will be explained.

The influence of resolving ballistic dispersion on near-surface concentration is investigated. Figure 9b shows $(\langle c_{0.02} \rangle / c_{\mathrm{BL}})_{\mathrm{UM55}} / (\langle c_{0.02} \rangle / c_{\mathrm{BL}})_{\mathrm{UKV}}$, the ratio of the UM55 to UKV $\langle c \rangle / c_{\mathrm{BL}}$ at $z/\langle z_i \rangle = 0.02$ at 1300 UTC. The ratio is calculated in analysis region 2 at 0.5-km intervals downstream of the southern edge of the source. At $D = 1$ km, the proportion of passive scalar at the surface in UM55 is ≈ 20% lower than in UKV. This is likely a consequence of differences in vertical grid resolution near the surface. By $D = 8$ km, the ratio has decreased from ≈ 0.8 to ≈ 0.53. Using an average CBL advection speed of $U \approx 6\ \mathrm{m\ s^{-1}}$ (Figure 2c), this corresponds to air that has been travelling ≈ 22 min since crossing the southern edge of the continuous source region. For UM55, this agrees well with $\tau_\Omega/2$ (Table 3) and the time at which the largest amounts of passive scalar are lofted in the CBL in Figure 7c. This is consistent with UM55 resolving ballistic dispersion, causing UM55 to have lower near-surface concentration compared with UKV at $D \approx 8$ km.

For $D > 8$ km, the proportion of passive scalar at the surface in UM55 relative to UKV starts to increase again. Although the emission of passive scalar and ballistic mixing at short times continues downstream, the proportion of passive scalar that has had long enough to become well mixed increases.

By explicitly resolving rather than parameterising vertical mixing within the CBL, up to 34% $(100 \times (0.53 - 0.80)/0.80)$ decreases in near-surface concentration can be expected. If the parameterised vertical mixing efficiency in UKV were increased, it is possible that $(\langle c_{0.02} \rangle / c_{\mathrm{BL}})_{\mathrm{UM55}} / (\langle c_{0.02} \rangle / c_{\mathrm{BL}})_{\mathrm{UKV}}$ would be closer to 1, since the parameterised near-surface concentrations would be lower. However, the minimum in $(\langle c_{0.02} \rangle / c_{\mathrm{BL}})_{\mathrm{UM55}} / (\langle c_{0.02} \rangle / c_{\mathrm{BL}})_{\mathrm{UKV}}$ at $D \approx U\tau_\Omega/2$ would still occur. The K-theory vertical mixing parameterisation used in many NWP and AQM schemes (Kukkonen et al., 2012) cannot produce the elevated concentrations in the upper CBL, since quantities cannot be transported against their local vertical gradient. "Countergradient" schemes, which are examples of "nonlocal" vertical mixing parametrisations, aim to represent the BL-scale coherent convective motions that lead to "lift-off" behaviour. The lift-off behaviour (where passive scalar is preferentially transported to the upper BL) is a consequence of passive scalar transport by coherent motions at short times since release (i.e., the $t \ll \tau$ ballistic dispersion limit). Simple gamma-type countergradient parameterisations (i.e., those with similar form to the second term on the right-hand side of Equation 2: Deardorff, 1972a; Lock et al., 2016) do not move quantities preferentially from the ground to the upper (rather than the lower) CBL. It is possible that TKE (Ito et al., 2015; Mellor & Yamada, 1982) or eddy-diffusion mass-flux (Pergaud et al., 2009; Siebesma et al., 2007) CBL turbulence schemes could represent this ballistic dispersion behaviour, but, to the authors' best knowledge, whether they do so accurately has not been investigated.

Lift-off behaviour can be expected to have the largest influence on near-surface air-pollution concentration

when there is a low proportion of well-mixed pollution: for example, when there is low background pollution concentration (i.e., little long-range transported pollution) and at short distances downstream ($D \approx Ut_\Omega/2$) of a strong source. The lifetime of individual pollutant species can also be expected to have an effect.

4 | CONCLUSIONS

CBL dispersion of passive scalar from a homogeneous city-scale ground source is simulated using hectometre- and kilometre-scale horizontal grid length NWP. We explain the differences in vertical mixing between these scales, develop a reduced analytical model to quantify differences in vertical mixing efficiency, and demonstrate that, for certain conditions, resolving "ballistic" type dispersion can have a leading-order effect on city-scale near-surface pollution concentration. The case study (May 4, 2016) is centred on London and has clear-sky conditions, with simulated $\langle z_i \rangle = 1.4$–$1.6$ km (1100–1400 UTC) and $-\langle z_i \rangle / L_O \approx 30$.

CBL turbulent mixing of scalar in UKV ($\Delta = \mathcal{O}(1\text{ km})$) is subgrid and therefore parameterised, so the passive scalar field varies smoothly in the horizontal. However, in UM100 and UM55 ($\Delta = \mathcal{O}(100\text{ m})$) the majority of CBL vertical turbulent mixing is resolved above the surface layer. Passive scalar converges near the surface and ascends in updrafts, before spreading horizontally at the capping inversion. This results in large passive scalar horizontal heterogeneity (e.g., for the continuous-release source, 2.6% of values are $> 1.64\langle c \rangle$ at $z/\langle z_i \rangle = 0.1$ (Section 3.1.2)).

The vertical mixing of passive scalar in UKV is parameterised using K theory, where movement of particles follows local concentration gradients (i.e., "diffusive" dispersion). For the hour following puff (i.e., instantaneous) release of passive scalar at the ground, this means that the concentration decreases and increases in the lower and upper CBL, respectively. However, in UM100 and UM55, where CBL-scale overturning eddies are resolved, particles undergo ballistic as well as diffusive dispersion. For times of the order of the turbulence memory timescale, particles retain memory of the eddy they are released into. The largest eddies transport particles into the upper CBL preferentially over the lower CBL. This "lift-off" behaviour for times $\mathcal{O}(\tau_\Omega/2 \sim 20\text{ min})$ results in higher concentration in the upper than the lower BL. To the best of our knowledge, this is the first time that lift-off behaviour has been demonstrated using NWP.

Starting from Langevin's equation, a reduced analytical model that takes the form of a damped simple harmonic oscillator is developed. It predicts the CoM trajectory of the puff-released passive scalar. The CoM increases ever more slowly with time from the ground towards $z/\langle z_i \rangle = 0.5$ for UKV, but it overshoots $z/\langle z_i \rangle = 0.5$ (due to ballistic dispersion) before tending towards $z/\langle z_i \rangle = 0.5$ for UM100 and UM55. This dispersion behaviour is captured by the overdamped (UKV) and underdamped (UM100/UM55) solutions with remarkable accuracy for such a simple model. The overdamped and underdamped solutions each have two timescales. UKV has two e-folding timescales, one longer (33.6 min) than the other (8.4 min), explaining why the vertical mixing is efficient initially but becomes less efficient with time. UM100 and UM55 have one e-folding timescale (≈ 10 min) that is much shorter than the longer UKV timescale, which explains why, at very short times (0–5 min), their vertical mixing is less efficient than UKV, but for greater times their vertical mixing is approximately three times more efficient. The other vertical mixing timescale for UM100 and UM55 is ≈ 40 min and represents the frequency of the CoM oscillations. With increasing time, the vertical concentration gradient reduces in all models, which makes UKV less efficient at vertical mixing, but UM100 and UM55 keep mixing efficiently due to the resolved (often counter-concentration-gradient) CBL overturning eddy transport.

Qualitatively, from horizontal (Figure 4) and vertical (Figure 3) cross-sections it is seen that more fine-detail structure in both the vertical velocity and passive scalar concentration fields is resolved in UM55 than in UM100. Using two-point cross-correlation functions (Figure 5) it is demonstrated that, near the top of the surface layer ($z/\langle z_i \rangle = 0.1$), the integral-scale turbulence is slightly larger in UM100 than in UM55. However, at $z/\langle z_i \rangle = 0.5$ the integral-scale turbulence has similar size in UM100 and UM55, suggesting that in the middle of the mixed layer the integral-scale turbulence has converged or is close to converging with Δ. The fact that the integral-scale turbulence in UM100 and UM55 is similarly well resolved in the mixed layer is consistent with UM100 and UM55 having qualitatively similar dispersion behaviour (e.g., Figures 2a,c, 7,8) and similar vertical mixing timescales (Table 3).

For an idealised source representing city-scale pollution emissions, it is demonstrated that representing ballistic-type dispersion reduces near-surface passive scalar concentration by up to 34%. At $\sim U\tau_\Omega/2 = 8$ km downstream of the upstream edge of the sources, the emissions occurring near the upstream edge have had time to be lifted into the upper CBL, and thus there is time for a reduction in near-surface concentration to develop. This lift-off behaviour can be expected to have its greatest influence on near-surface air-pollution concentration when contributions to the concentration

are dominated by local emissions (e.g., for strong city emissions with low-concentration air transported in by mesoscale/synoptic-scale flow).

Given that the turbulent structure of the CBL is influenced by the amount of surface sensible heating and wind shear, it would be worth investigating other atmospheric conditions to find out whether the NWP dispersion behaviour exhibited here holds more generally. For example, does UM100 still behave similarly to UM55 for less convective conditions and during the morning neutral/convective transition, when z_i and the turbulence integral scales are smaller? Also, more realistic scenarios that include chemistry and heterogeneous pollution sources could be investigated, to see if ballistic-type dispersion still has a large influence on near-surface concentrations. There is evidence that the roughness of the urban surface makes horizontal convective rolls more likely than over rural areas (Miao & Chen, 2008), and that anthropogenic heat emissions in cities can cause weakly convective conditions to occur more often at night (chap. 7, Oke et al., 2017). Therefore, the extent to which the urban increment changes resolved passive scalar dispersion is of interest. The MetUM does not have a countergradient vertical mixing term for passive scalars. Inclusion of such a term would likely increase parametrised CBL vertical mixing efficiency, so that the UKV and UM100/UM55 vertical mixing efficiencies become more similar. However, current countergradient parameterisations used in NWP (e.g., Lock et al., 2000; Pleim & Chang, 1992) do not move passive scalar preferentially to the upper (over the lower) CBL, so do not fully represent the dispersion behaviour caused by ballistic dispersion. Assuming that representation of ballistic-type dispersion is important for predicting surface-level concentrations in general, new CBL vertical mixing parameterisations (e.g., based on fractional calculus: Paradisi et al., 2001) should be developed for NWP.

AUTHOR CONTRIBUTIONS

Lewis P. Blunn: conceptualization; data curation; formal analysis; investigation; methodology; software; visualization; writing – original draft; writing – review and editing. **Robert S. Plant:** conceptualization; funding acquisition; methodology; project administration; resources; supervision; writing – review and editing. **Omduth Coceal:** conceptualization; methodology; project administration; resources; supervision; writing - review and editing. **Sylvia I. Bohnenstengel:** conceptualization; funding acquisition; methodology; project administration; resources; software; supervision; writing – review and editing. **Humphrey W. Lean:** conceptualization; funding acquisition; methodology; project administration; resources; supervision; writing – review and editing. **Janet F. Barlow:** conceptualization; funding acquisition; methodology; project administration; resources; supervision; writing – review and editing.

ACKNOWLEDGEMENTS

Lewis P. Blunn was joint funded by NCAS and the University of Reading on an Air Pollution Science Training Studentship Programme and was part of the Met Office Academic Partnership (MOAP). We acknowledge the use of the MONSooN system, a collaborative facility supplied under the Joint Weather and Climate Research Programme, which is a strategic partnership between the Met Office and the Natural Environment Research Council (NERC).

ORCID

Lewis P. Blunn https://orcid.org/0000-0002-3207-5002
Robert S. Plant https://orcid.org/0000-0001-8808-0022
Omduth Coceal https://orcid.org/0000-0003-0705-6755
Sylvia I. Bohnenstengel https://orcid.org/0000-0001-6170-5774
Humphrey W. Lean https://orcid.org/0000-0002-1274-4619
Janet F. Barlow https://orcid.org/0000-0002-9022-6833

REFERENCES

Baklanov, A., Schlünzen, K., Suppan, P., Baldasano, J., Brunner, D., Aksoyoglu, S. et al. (2014) Online coupled regional meteorology chemistry models in Europe: current status and prospects. *Atmospheric Chemistry and Physics*, 14, 317–398.

Belair, S., Leroyer, S., Seino, N., Spacek, L., Souvanlassy, V. & Paquin-Ricard, D. (2018) Role and impact of the urban environment in a numerical forecast of an intense summertime precipitation event over Tokyo. *Journal of the Meteorological Society of Japan Series II*, 96A, 77–94.

Best, M., Pryor, M., Clark, D., Rooney, G., Essery, R., Ménard, C. et al. (2011) The joint UK land environment simulator (JULES), model description–part 1: energy and water fluxes. *Geoscientific Model Development*, 4, 677–699.

Blunn, L.P. (2021) *Characterising mixing and pollution transport in the urban boundary layer*. PhD thesis. Reading: University of Reading.

Bohnenstengel, S., Evans, S., Clark, P.A. & Belcher, S. (2011) Simulations of the London urban heat island. *Quarterly Journal of the Royal Meteorological Society*, 137, 1625–1640.

Boutle, I., Eyre, J. & Lock, A. (2014) Seamless stratocumulus simulation across the turbulent gray zone. *Monthly Weather Review*, 142, 1655–1668.

Boutle, I., Finnenkoetter, A., Lock, A. & Wells, H. (2016) The London model: forecasting fog at 333 m resolution. *Quarterly Journal of the Royal Meteorological Society*, 142, 360–371.

Cimorelli, A.J., Perry, S.G., Venkatram, A., Weil, J.C., Paine, R.J., Wilson, R.B. et al. (2005) AERMOD: a dispersion model for industrial source applications. Part I: general model formulation and boundary layer characterization. *Journal of Applied Meteorology*, 44, 682–693.

Clark, D., Mercado, L., Sitch, S., Jones, C., Gedney, N., Best, M. et al. (2011) The joint UK land environment simulator (JULES), model description–part 2: carbon fluxes and vegetation dynamics. *Geoscientific Model Development*, 4, 701–722.

Crawford, B., Grimmond, C.S.B., Ward, H.C., Morrison, W. & Kotthaus, S. (2017) Spatial and temporal patterns of surface–atmosphere energy exchange in a dense urban environment using scintillometry. *Quarterly Journal of the Royal Meteorological Society*, 143, 817–833.

Davies, T., Cullen, M.J., Malcolm, A.J., Mawson, M., Staniforth, A., White, A. et al. (2005) A new dynamical core for the Met Office's global and regional modelling of the atmosphere. *Quarterly Journal of the Royal Meteorological Society*, 131, 1759–1782.

Deardorff, J. (1972a) Theoretical expression for the countergradient vertical heat flux. *Journal of Geophysical Research*, 77, 5900–5904.

Deardorff, J.W. (1970) Preliminary results from numerical integrations of the unstable planetary boundary layer. *Journal of the Atmospheric Sciences*, 27, 1211–1213.

Deardorff, J.W. (1972b) Numerical investigation of neutral and unstable planetary boundary layers. *Journal of the Atmospheric Sciences*, 29, 91–115.

Dosio, A., Guerau de Arellano, J.V., Holtslag, A.A. & Builtjes, P.J. (2005) Relating Eulerian and Lagrangian statistics for the turbulent dispersion in the atmospheric convective boundary layer. *Journal of the Atmospheric Sciences*, 62, 1175–1191.

Dosio, A., Vilà-Guerau de Arellano, J., Holtslag, A.A. & Builtjes, P.J. (2003) Dispersion of a passive tracer in buoyancy-and shear-driven boundary layers. *Journal of Applied Meteorology*, 42, 1116–1130.

Garratt, J. (1994) *The atmospheric boundary layer*. Cambridge: Cambridge University Press.

Gopalakrishnan, S. & Avissar, R. (2000) An LES study of the impacts of land surface heterogeneity on dispersion in the convective boundary layer. *Journal of the Atmospheric Sciences*, 57, 352–371.

Hagelin, S., Auger, L., Brovelli, P. & Dupont, O. (2014) Nowcasting with the AROME model: first results from the high-resolution AROME airport. *Weather and Forecasting*, 29, 773–787.

Halliwell, C. (2017) Subgrid turbulence scheme. Unified Model documentation paper 28, Met Office.

Hanley, K.E., Barrett, A.I. & Lean, H.W. (2016) Simulating the 20 May 2013 Moore, Oklahoma tornado with a 100-metre grid-length NWP model. *Atmospheric Science Letters*, 17, 453–461.

Hanley, K.E., Plant, R.S., Stein, T.H., Hogan, R.J., Nicol, J.C., Lean, H.W. et al. (2015) Mixing-length controls on high-resolution simulations of convective storms. *Quarterly Journal of the Royal Meteorological Society*, 141, 272–284.

Honnert, R., Efstathiou, G.A., Beare, R.J., Ito, J., Lock, A., Neggers, R. et al. (2020) The atmospheric boundary layer and the "Gray Zone" of turbulence: a critical review. *Journal of Geophysical Research: Atmospheres*, 125, e2019JD030317.

Honnert, R., Masson, V. & Couvreux, F. (2011) A diagnostic for evaluating the representation of turbulence in atmospheric models at the kilometric scale. *Journal of the Atmospheric Sciences*, 68, 3112–3131.

Ito, J., Niino, H., Nakanishi, M. & Moeng, C.-H. (2015) An extension of the Mellor–Yamada model to the terra incognita zone for dry convective mixed layers in the free convection regime. *Boundary-Layer Meteorology*, 157, 23–43.

Kotthaus, S. & Grimmond, C.S.B. (2014) Energy exchange in a dense urban environment–part 1: temporal variability of long-term observations in Central London. *Urban Climate*, 10, 261–280.

Kukkonen, J., Olsson, T., Schultz, D.M., Baklanov, A., Klein, T., Miranda, A.I. et al. (2012) A review of operational, regional-scale, chemical weather forecasting models in Europe. *Atmospheric Chemistry and Physics*, 12, 1–87.

Lean, H.W., Barlow, J.F. & Clark, P.A. (2022) The use of 100 m scale NWP models to understand differences between different measures of mixing height in a morning growing clear convective boundary layer over London. *Quarterly Journal of the Royal Meteorological Society*, 148, 1983–1995.

Lean, H.W., Barlow, J.F. & Halios, C.H. (2019) The impact of spin-up and resolution on the representation of a clear convective boundary layer over London in order 100 m grid-length versions of the Met Office Unified Model. *Quarterly Journal of the Royal Meteorological Society*, 145, 1674–1689.

Leroyer, S., Bélair, S., Husain, S.Z. & Mailhot, J. (2014) Subkilometer numerical weather prediction in an urban coastal area: a case study over the Vancouver metropolitan area. *Journal of Applied Meteorology and Climatology*, 53, 1433–1453.

Leroyer, S., Bélair, S., Souvanlasy, V., Vallée, M., Pellerin, S. & Sills, D. (2022) Summertime assessment of an urban-scale numerical weather prediction system for Toronto. *Atmosphere*, 13, 1030.

Lilly, D.K. (1962) On the numerical simulation of buoyant convection. *Tellus*, 14, 148–172.

Lilly, D.K. (1968) Models of cloud-topped mixed layers under a strong inversion. *Quarterly Journal of the Royal Meteorological Society*, 94, 292–309.

Lock, A., Brown, A., Bush, M., Martin, G. & Smith, R. (2000) A new boundary layer mixing scheme. Part I: scheme description and single-column model tests. *Monthly Weather Review*, 128, 3187–3199.

Lock, A., Edwards, J. & Boutle, I. (2016) The parametrization of boundary layer processes. Unified Model documentation paper 24, Met Office.

Luhar, A.K. & Britter, R.E. (1989) A random walk model for dispersion in inhomogeneous turbulence in a convective boundary layer. *Atmospheric Environment*, 23, 1911–1924.

McHugh, C., Carruthers, D. & Edmunds, H. (1997) ADMS-urban: an air quality management system for traffic, domestic and industrial pollution. *International Journal of Environment and Pollution*, 8, 666–674.

Mellor, G.L. & Yamada, T. (1982) Development of a turbulence closure model for geophysical fluid problems. *Reviews of Geophysics*, 20, 851–875.

Miao, S. & Chen, F. (2008) Formation of horizontal convective rolls in urban areas. *Atmospheric Research*, 89, 298–304.

Monin, A. & Yaglom, A. (1975) *Statistical fluid mechanics: mechanics of turbulence*. Cambridge, MA: MIT Press.

Oke, T.R., Mills, G. & Voogt, J. (2017) *Urban climates*. Cambridge: Cambridge University Press.

Paradisi, P., Cesari, R., Mainardi, F., Maurizi, A. & Tampieri, F. (2001) A generalized Fick's law to describe non-local transport effects. *Physics and Chemistry of the Earth, Part B: Hydrology, Oceans and Atmosphere*, 26, 275–279.

Pergaud, J., Masson, V., Malardel, S. & Couvreux, F. (2009) A parameterization of dry thermals and shallow cumuli for mesoscale numerical weather prediction. *Boundary-Layer Meteorology*, 132, 83–106.

Pleim, J.E. (2007) A combined local and nonlocal closure model for the atmospheric boundary layer. Part I: model description and testing. *Journal of Applied Meteorology and Climatology*, 46, 1383–1395.

Pleim, J.E. & Chang, J.S. (1992) A non-local closure model for vertical mixing in the convective boundary layer. *Atmospheric Environment. Part A. General Topics*, 26, 965–981.

Porson, A., Clark, P.A., Harman, I., Best, M. & Belcher, S. (2010) Implementation of a new urban energy budget scheme in the MetUM. Part I: description and idealized simulations. *Quarterly Journal of the Royal Meteorological Society*, 136, 1514–1529.

Ronda, R., Steeneveld, G., Heusinkveld, B., Attema, J. & Holtslag, A. (2017) Urban finescale forecasting reveals weather conditions with unprecedented detail. *Bulletin of the American Meteorological Society*, 98, 2675–2688.

Salesky, S.T., Chamecki, M. & Bou-Zeid, E. (2017) On the nature of the transition between roll and cellular organization in the convective boundary layer. *Boundary-Layer Meteorology*, 163, 41–68.

Schmidt, H. & Schumann, U. (1989) Coherent structure of the convective boundary layer derived from large-eddy simulations. *Journal of Fluid Mechanics*, 200, 511–562.

Siebesma, A.P., Soares, P.M. & Teixeira, J. (2007) A combined eddy-diffusivity mass-flux approach for the convective boundary layer. *Journal of the Atmospheric Sciences*, 64, 1230–1248.

Smagorinsky, J. (1963) General circulation experiments with the primitive equations: 1. The basic experiment. *Monthly Weather Review*, 91, 99–164.

Stockie, J.M. (2011) The mathematics of atmospheric dispersion modeling. *SIAM Review*, 53, 349–372.

Tang, Y., Lean, H.W. & Bornemann, J. (2013) The benefits of the Met Office variable resolution NWP model for forecasting convection. *Meteorological Applications*, 20, 417–426.

Taylor, G.I. (1922) Diffusion by continuous movements. *Proceedings of the London Mathematical Society*, 2, 196–212.

Tennekes, H. (1979) The exponential Lagrangian correlation function and turbulent diffusion in the inertial subrange. *Atmospheric Environment*, 13, 1565–1567.

Thomson, D. (1987) Criteria for the selection of stochastic models of particle trajectories in turbulent flows. *Journal of Fluid Mechanics*, 180, 529–556.

Thomson, D. & Wilson, J. (2012) History of Lagrangian stochastic models for turbulent dispersion. *Lagrangian Modeling of the Atmosphere*, 200, 19–36.

Warhaft, Z. (2000) Passive scalars in turbulent flows. *Annual Review of Fluid Mechanics*, 32, 203–240.

Webster, H. & Thomson, D. (2018) *NAME – model description*. Exeter: UK Met Office: User Guide for NAME.

Weil, J. (1990) A diagnosis of the asymmetry in top-down and bottom-up diffusion using a Lagrangian stochastic model. *Journal of the Atmospheric Sciences*, 47, 501–515.

Willis, G. & Deardorff, J. (1976) A laboratory model of diffusion into the convective planetary boundary layer. *Quarterly Journal of the Royal Meteorological Society*, 102, 427–445.

Willis, G. & Deardorff, J. (1979) Laboratory observations of turbulent penetrative-convection planforms. *Journal of Geophysical Research: Oceans*, 84, 295–302.

Willis, G.E. & Deardorff, J.W. (1981) A laboratory study of dispersion from a source in the middle of the convectively mixed layer. *Atmospheric Environment*, 15, 109–117.

Wilson, J.D. & Sawford, B.L. (1996) Review of Lagrangian stochastic models for trajectories in the turbulent atmosphere. *Boundary-Layer Meteorology*, 78, 191–210.

Wood, N., Staniforth, A., White, A., Allen, T., Diamantakis, M., Gross, M. et al. (2014) An inherently mass-conserving semi-implicit semi-Lagrangian discretization of the deep-atmosphere global non-hydrostatic equations. *Quarterly Journal of the Royal Meteorological Society*, 140, 1505–1520.

Wyngaard, J.C. (2004) Toward numerical modeling in the "Terra Incognita". *Journal of the Atmospheric Sciences*, 61, 1816–1826.

Wyngaard, J.C. & Brost, R.A. (1984) Top-down and bottom-up diffusion of a scalar in the convective boundary layer. *Journal of the Atmospheric Sciences*, 41, 102–112.

How to cite this article: Blunn, L.P., Plant, R.S., Coceal, O., Bohnenstengel, S.I., Lean, H.W. & Barlow, J.F. (2024) The influence of resolved convective motions on scalar dispersion in hectometric-scale numerical weather prediction models. *Quarterly Journal of the Royal Meteorological Society*, 1–19. Available from: https://doi.org/10.1002/qj.4632

APPENDIX A. REDUCTION OF THE GENERALISED LANGEVIN EQUATION TO A DAMPED SIMPLE HARMONIC OSCILLATOR

In this section, the generalised Langevin equation (Thomson & Wilson, 2012) is reduced to a DSHO describing the CoM evolution of particles puff-released at some height in the CBL. In Section 3.3 the DSHO is solved and used to estimate vertical mixing timescales for UKV, UM100, and UM55.

LSMs are able to produce the correct dispersion behaviour in the diffusive and ballistic limits. The generalised Langevin equation is the usual starting point for modern LSMs, and for vertical dispersion is given by (Thomson, 1987)

$$dw = a(z, w, t)\ dt + b(z, w, t)\ d\xi, \tag{A1}$$

where $d\xi$ are random velocity increments and a and b are functions that need to be parameterised. Once w (the vertical velocity of the particle) has been determined, one can integrate $dz = w\,dt$ to find the particle position.

The second term on the right-hand side of Equation A1 is the diffusion term and represents the small-scale turbulent motions. Thomson (1987) showed that the random velocity increments must be Gaussian if w is to evolve continuously in time without jumps. More specifically, $d\xi$ becomes a Gaussian random forcing with zero mean and

variance dt. b is generally taken to be

$$b = (C_0\epsilon)^{1/2}, \tag{A2}$$

so that it is consistent with the Lagrangian structure function in the inertial subrange (Weil, 1990). C_0 is often treated as a dispersion parameter, but more strictly is a universal constant (Monin and Yaglom, 1975), and ϵ is the local ensemble-averaged dissipation rate (Weil, 1990). It is common to express b in terms of the decorrelation timescale $\tau = 2\sigma_w^2/(C_0\epsilon)$, so that $b = (2\sigma_w^2/\tau)^{1/2}$ (Tennekes, 1979; Thomson & Wilson, 2012).

It is well known in CBLs that vertical velocity probability density functions (PDFs) are positively skewed (Weil, 1990). However, to obtain a reduced analytical model we assume Gaussian vertical velocity PDFs throughout the CBL and note that asymmetries between updrafts and downdrafts and between the lower and upper BL will not be represented. For stationary, horizontally homogeneous flows, with Gaussian vertical velocity PDF (Thomson, 1987; Weil, 1990),

$$a = -\frac{C_0\epsilon w}{2\sigma_w^2} + \frac{1}{2}\left(1 + \frac{w^2}{\sigma_w^2}\right)\frac{\partial\sigma_w^2}{\partial z}. \tag{A3}$$

The first term on the right-hand side of Equation A3 is the damping term and represents the fading memory of the turbulence. This can be seen by writing it in terms of the decorrelation timescale so that it equals $-w/\tau$. The second term on the right-hand side of Equation A3 is the so called drift term and offsets the tendency of simulated particles to accumulate in areas of low σ_w.

Let us take Equations A1–A3 as the starting point for the reduced analytical model. Except near the ground and the top of the CBL, the ensemble average of the second term on the right-hand side of Equation A1 is zero, since the Gaussian forcing has equal probability of displacing particles upwards and downwards. This term will be neglected. The drift term simplifies upon ensemble averaging, so that Equations A1–A3 can be written as

$$\ddot{\tilde{z}} = -\frac{\dot{\tilde{z}}}{\tau} + \frac{\partial\sigma_w^2}{\partial z}, \tag{A4}$$

where $\tilde{z}$ is the ensemble average particle position (or CoM of the particles). We assume that τ is constant, which is likely a poorer assumption near the ground and top of the CBL, where turbulence characteristics are most different compared with the rest of the CBL.

Turbulence is not vertically homogeneous in the CBL, otherwise the drift term in Equation A4 would be zero and the characteristic lift-off behaviour of puff-released passive scalars near the surface would not be reproduced (Luhar & Britter, 1989; Weil, 1990). Passive scalar would not spread faster than $\langle z^2\rangle \propto t$ at times shortly after release. For a CBL, the damping and drift terms on the right-hand side of Equation A4 are of the same order of magnitude, so both should be represented. Here, a heuristic approximation is made to the drift term, allowing some representation of the vertical heterogeneity in CBL turbulence, even though it is neglected in the damping term and diffusion term (second term on the right-hand side of Equation A1). In CBL turbulence, σ_w^2 tends to have a maximum at approximately $\langle z_i\rangle/2$ (Salesky et al., 2017). The drift term is therefore positive and negative in the bottom and top halves of the CBL, respectively, and acts to move particles towards $\langle z_i\rangle/2$. It is as if the drift term is a restoring force. On this basis the drift term will be represented as being proportional to the negative displacement from the middle of the CBL.

Another argument for representing the drift term as a restoring force can be made. The main energy-producing eddies under convective conditions span the entire CBL depth, and might be roughly approximated as circular in an x–z plane. A particle released into such an eddy (in the absence of the influence of other eddies) would undergo perpetual circular motions with angular frequency ω analogous to simple harmonic motion when projected onto the z-axis.

The LSM has been reduced to a DSHO of the form

$$\ddot{\tilde{z}} = -2\gamma\dot{\tilde{z}} - \omega^2(\tilde{z} - \langle z_i\rangle/2), \tag{A5}$$

where $\omega = 2\pi/\tau_\omega$ is the natural frequency, τ_ω is expected to be of the order of the eddy turnover timescale, and $\gamma = 1/(2\tau)$ determines the amount of damping. The first and second terms on the right-hand side are the damping and restoring forces, respectively. The $-\langle z_i\rangle/2$ factor places the DSHO equilibrium at the middle of the BL. Note that the time derivative and ensemble average operator orders have been swapped from Equation A4, assuming that they commute, at least to a reasonable approximation.